Draft version November 7, 2018
Preprint typeset using LaTeX style emulateapj v. 11/12/01

DEEP CHANDRA AND MULTICOLOR HST OBSERVATIONS OF THE JETS OF 3C 371 AND PKS 2201+044

Rita M. Sambruna, Davide Donato
NASA/GSFC, Code 661, Greenbelt, MD 20771 (Rita.M.Sambruna@nasa.gov)

F. Tavecchio and L. Maraschi
Osservatorio Astronomico di Brera, via Brera 28, 20121 Milano, Italy

C. C. Cheung[1]
Kavli Institute for Particle Astrophysics and Cosmology, Stanford University, Stanford, CA 94305

C. Megan Urry
Yale University, New Haven, CT 06520
Draft version November 7, 2018

ABSTRACT

This paper presents multiwavelength imaging and broad-band spectroscopy of the relativistic jets in the two nearby radio galaxies 3C 371 and PKS 2201+044, acquired with *Chandra*, *HST*, *VLA*, and *MERLIN*. Radio polarization images are also available. The two sources stand out as "intermediate" between FRIs and FRIIs; their cores are classified as BL Lacs, although broad and narrow optical emission lines were detected at times. The multiwavelength images show jet morphologies with the X-ray emission peaking closer to the nucleus than the longer wavelengths. The jets are resolved at all wavelengths in a direction perpendicular to the jet axis. The jets SEDs are consistent with a single spectral component from radio to X-rays, interpreted as synchrotron emission. The SEDs show a progressive softening from the inner to the outer regions of the jet, indicating that the electron break energy moves to lower energies with distance from the core. Overall, the X-ray and multiwavelength properties of the jets of 3C 371 and PKS 2201+044 appear intermediate between those of FRIs and FRIIs.

Subject headings: Galaxies: active — galaxies: jets — (galaxies:) blazars: individual — X-rays: galaxies

1. INTRODUCTION

Recent studies of extragalactic radio jets with *Chandra* and *HST* demonstrated the power of multiwavelength imaging spectroscopy to understand the physical properties and structure of these systems. These observations established that the X-ray morphology and emission processes of kpc-scale jets are closely related to radio morphology. In low-power Fanaroff-Riley I (FRIs; Fanaroff & Riley 1974) radio galaxies, the X-ray emission falls off more rapidly away from the core than does the longer wavelength emission; the jet radio-to-X-ray Spectral Energy Distributions (SEDs) can be described by single or broken power law spectra (Worrall et al. 2003), suggesting the X-ray emission from these jets is due to synchrotron radiation from the same electron population responsible for the radio.

In higher-power FRIIs, the X-ray jet morphology often follows very closely the radio one (Sambruna et al. 2002, 2004, 2006; Marshall et al. 2005) and individual knots have complex SEDs with X-ray flux above the extrapolation from the optical. In 3C 273, however, the connection between optical and X-ray spectra from the jet knots is unclear allowing different interpretations (Uchiyama et al. 2006). The origin of the X-ray emission is still debated, ranging from inverse Compton emission off the CMB (IC/CMB; Tavecchio et al. 2000; Celotti et al. 2001) to synchrotron emission from an electron population with an excess of high-energy particles resulting from acceleration (Stawarz et al. 2004) or losses limited by Klein-Nishina effects (Dermer & Atoyan 2002), to synchrotron emission from protons (Aharonian 2002). In some sources, the X-ray jets peak upstream from the radio and optical (Sambruna et al. 2006), suggesting deceleration by entrainment of ambient gas in the context of IC/CMB (Georganopoulos & Kazanas 2004; Tavecchio et al. 2006). Thermal emission from shocked ambient gas hit by the relativistic jet is also observed (Ly et al. 2005), allowing to derive the gas density and the jet speed.

Interestingly, high-energy emission was also detected from the jets of a few BL Lacertae sources, traditionally unified to FRIs (Wardle, Moore, & Angel 1984; Kollgaard et al. 1992). Early *Chandra* observations detected X-ray counterpart to the optical jet of PKS 0521–365 (Birkinshaw et al. 2002), where the broad-band emission was found to be consistent with synchrotron emission from a broken power law populations of electrons, similar to FRIs. Another X-ray jet was detected by us (Pesce et al. 2001, P01 in the following) in a short (10 ks) ACIS-S exposure of 3C 371 aimed at studying the circumnuclear environment (Donato, Sambruna, & Gliozzi 2004). We found evidence for a synchrotron origin of the X-ray emission from an electron population with decreasing high-energy cutoff; however, the ACIS-S exposure was too short to study the X-ray jet properties in detail, in particular the X-ray morphology and spectra. An X-ray jet is also detected in 2007+777 in our ACIS-S image (Sambruna et al. 2007).

We later acquired deeper *Chandra* and multicolor HST

[1] Jansky Postdoctoral Fellow; National Radio Astronomy Observatory

observations of 3C 371 and PKS 2201+044, which are the focus of this paper. The two sources were classified as BL Lacs on the basis of their non-thermal continuum properties, although optical emission lines are detected (see § 2.1). In both cases, the core-jet radio morphology resembles that of FRIIs; however, their radio power and the optical magnitude of their hosts (Urry et al. 2000) firmly put them in the FRI region of the Owen-Ledlow plane (Ledlow & Owen 1996). As part of our program of multi-wavelength imaging-spectroscopy of kpc-scale jets, we obtained deep *Chandra* and multicolor *HST* observations of both 3C 371 and PKS 2201+044. Here we present the X-ray and optical observations, as well as new radio data.

The paper is structured as follows. Observations and sources properties are summarized in § 2. The results for the cores and jets are given in §§ 3 and 4, respectively, while discussion and conclusions follow in § 5. Throughout this paper, a concordance cosmology with $H_0 = 71$ km s^{-1} Mpc^{-1}, Ω_Λ=0.73, and Ω_m=0.27 (Spergel et al. 2003) is adopted. With this choice, 1″ corresponds to 0.983 kpc for 3C 371 and to 0.535 kpc for PKS 2201+044. The energy spectral index, α, is defined such that $F_\nu \propto \nu^{-\alpha}$, and the photon index $\Gamma = \alpha + 1$.

2. OBSERVATIONS

2.1. *The sources*

3C 371: This is a nearby (z=0.051) radio source, optically classified as a BL Lac based on variability and polarization (Angel & Stockman 1980). It was previously classified as an N galaxy (Miller 1975), based on the presence of narrow optical emission lines in the spectrum. Its radio morphology is more similar to an FRII, with two giant lobes and a 25″-long, one-sided jet (Wrobel & Lind 1990; Kollgaard et al. 1996). The jet-to-counterjet flux ratio in the radio indicates 3C 371 is seen at moderate viewing angles, $\theta \leq 18°$ (Gomez & Marscher 2000).

An optical counterpart to the radio jet was detected in ground-based images (Nilsson et al. 1997) and with *HST* (Scarpa et al. 1999), while X-ray emission from the jet was discovered by us in an exploratory 10 ks *Chandra* observation (P01). The optical morphology of the jet is similar to the radio, with an inner weaker knot (knot B) at 1.9″ from the core, a brighter one (knot A) at 3.1″ (Scarpa et al. 1999). The X-ray image indicated a different morphology, with the jet emitting most of the X-ray counts at knot B and fading toward the end of the jet. In both knots, the X-ray flux lies below the extrapolation of the radio-to-optical continuum. We interpreted the SEDs in terms of synchrotron emission from a population of particles with a decreasing high-energy cutoff and moderate beaming (P01).

PKS 2201+044: This BL Lac is hosted by a prominent elliptical galaxy at z=0.027. At one time, its showed an optical spectrum typical of a Seyfert 1, with broad (Hα, Hβ) and narrow ([OI], [OIII]) emission lines (Veron-Cetty & Veron 1993). In the radio, it shows a core-jet morphology with total extension of 5.6′ (Ulvestad & Johnson 1984; Laurent-Muehleisen et al. 1993). A bright and compact radio feature was found at 2.2″ from the nucleus. Subsequent *HST* observations revealed an optical counterpart to the 2.2″ hot spot and additional candidate knots in the inner parts of the jet (Scarpa et al. 1999). The bright optical 2.2″ knot is resolved by *HST* in directions both parallel and perpendicular to the jet axis, with a complex structure.

2.2. *X-ray*

Chandra observed 3C 371 and PKS 2201+044 on 2002 August 8 and 2002 April 27, respectively. The live times were 40 ks and 38 ks, yielding 37 ks and 34.6 ks of useful exposure time after removing flaring background events that occured during the observations. The background light curves were extracted from source-free regions on the same chip of the source. The data were analyzed using standard screening criteria. In particular we used the version 3.3 of the `CIAO` software package and the latest calibration files provided by the *Chandra* X-ray Center (`CALDB v.3.2.1`).

Both sources were observed at the aim point of the S3 chip of the ACIS-S detector. Since the sources were expected to have a bright core, the 1/8 subarray mode (frame time of 0.44 s) was used to reduce the effect of the nuclear pileup. In a circular region of radius 1.5″ the counts rates of the cores of 3C 371 and PKS 2201+044 are 0.54 and 0.29 c/s, respectively. According to `PIMMS`, the estimated pileup percentages are relatively small, 8% and 4%, for the two sources. The two X-ray images show a readout streak on the S3 chip that has been removed by the `destreak` tool, for imaging purpose.

The cores fluxes and spectra were extracted using `panda` regions centered on the pixel with the highest counts. These regions, that resemble a pie with a slice removed, have an outer radius of 4″ and aperture angles of 260° and 270° for 3C 371 and PKS 2201+044, respectively. The aperture angles were chosen to avoid the jet contamination.

For the detected knots, fluxes and spectra were extracted from ellipses with axis lengths of 0.41″× 1.06″ for 3C 371, and 0.43″× 0.85″ for PKS 2201+044, respectively, centered on the radio positions and with the major axis oriented perpendicular to the jet. The corresponding aperture corrections are 2.7 for 3C 371, and 3.3 for PKS 2201+044. The sizes of the ellipses represent a compromise between the need to maximize the number of X-ray photons while at the same time covering an area similar to the regions used at radio and optical, where the angular resolution is better. For the innermost radio/optical knots α, where the contribution of the ACIS PSF's wings is likely to be strong, we used the same procedure. In all cases the background was evaluated in `panda` regions centered on the nucleus and with inner and outer radii such as to match the width of the source extraction region. The choice of this background region ensures that the contribution of the diffuse thermal emission and/or the wings of the PSF as a function of azimuth are averaged. Figures 1–4 show the ACIS-S images of the inner and outer jets.

The net count rates of the knots are reported in Table 1. We use the same nomenclature as specified in Scarpa et al. (1999) for the bright knots A and B in 3C 371 and A in PKS 2201+044, and the greek alphabet to identify the not previously named inner knots. For knots α, the closest to the core and only weakly detected, we only list conservatively a 3σ upper limit to the count rates. Knots β at 1.3″ and 1.6″ from the cores were detected at 3σ over the

background; for these, we also extracted ACIS spectra.

The ACIS spectra of the cores and the jet knots have been analyzed within `XSPEC v.11.3.2`. The spectra of components with a large number of counts (e.g., 100 or more) were grouped so that each new energy bin had at least 20 counts to enable the use of the χ^2 statistics. Errors quoted throughout are 90% for one parameter of interest ($\Delta\chi^2$=2.7). The unbinned X-ray spectra with <100 counts (i.e., knot A for 3C 371 and knots β and A for PKS 2201+044) were fitted using the C-statistic. The uncertainties on the X-ray counts, σ_N, were calculated according to the formula $\sigma_N = [(\sigma_S)^2 + (\sigma_B)^2]^{1/2}$, where σ_S and σ_B are the uncertainties of the source and the rescaled by area background, respectively. In the regime of low counts, to evaluate the uncertainties we adopted the formula in Gehrels (1986): $\sigma = 1 + (S + 0.75)^{1/2}$.

The X-ray fluxes for the individual knots are listed in Table 4. All fluxes are background-subtracted and corrected for finite aperture effects. They were also corrected for the expected contamination due to the PSF wings of nearby knots. The total correction factors are given in the Table.

2.3. *HST*

The sources were observed by us with the WFPC2 and STIS on *HST* in summer 2001. We also searched the *HST* archive and found additional data. 3C 371 has been the target of multiple observations related to 7 different proposals, from 1994 to 2005, including, besides our observations, images with Near-Infrared Camera and Multi-Object Spectrometer (NICMOS) and the Advanced Camera for Surveys (ACS), the latter published by Perlman et al. (2006). On the contrary, PKS 2201+044 was observed only with STIS and WFPC2 between 1998 and 2001. In many cases, the two sources were observed using different apertures and filters. The observation log of the *HST* observations considered in this paper is presented in Table 2.

We retrieved the data from the Multimission Archive at Space Telescope (MAST), reprocessed by the standard calibration pipeline. In particular, we downloaded the mosaic image of NICMOS, the flat-fielded images of ACS and STIS, and the c0f files of WFPC2. The subsequent reduction of the data was performed with the NOAO image processing software Image Reduction Analysis Facility (IRAF).

In the case of multiple exposures, we stacked them together, removing the cosmic rays with the CRREJ task. In the inner part of the radio jets the optical emission is contaminated and/or overwhelmed by the light of the host galaxy. With the tasks ELLIPSE and BMODEL we fitted the host emission using a two-dimensional elliptical galaxy model, after masking the jet and diffraction spike areas. The subtraction of the galaxy model from the stacked images revealed the complex morphology of the two jets also at optical wavelengths.

Close to the nucleus, the galaxy subtraction is likely to leave imperfections. Indeed, in Figure 1 the feature in F555W alongside knots β and B is most likely a residual of such an imperfect model, as it is not present in the other filters. In any case, it does not affect the measurement of the flux as the latter was extracted from a small region.

We used squared apertures centered on the radio jet position to extract the optical flux. Although the dimensions of these regions change very slightly from one *HST* detector to the other due to the difference in pixel size, they are of the order of $\sim$0.3″. In the case of knots A, which are resolved both longitudinally and transversally to the jet axis (see § 3), we used an extraction region with a total area similar to the X-ray extraction region, or 0.3 arcsec^2. The background was estimated using several identical apertures in adjacent regions to the extractions. Due to background variation, we used the average and standard deviation of the values estimated in the boxes.

Counts were converted to flux densities using the value in PHOTFLAM (the inverse sensitivity measurement) in the image headers. We corrected the extracted fluxes not only for the effects of the finite "aperture" but also for the Galactic extinction. The corrections for the finite aperture were derived using the profile of the encircled energy of each detector. For the Galactic extinction we fitted the values reported in NED (Schlegel, Finkbeiner, & Davis 1998) with a power law and we extrapolated the value corresponding to the pivot wavelength of each filter. In particular, the extinction corrections for 3C 371 were about 2% for NICMOS, 10% for ACS, 11% for WFPC2 (F555W), and 46% for STIS. For the observations of PKS 2201+044 we corrected the fluxes by 8% for STIS, 9% and 13% for WFPC2 (F702W and F555W, respectively). The optical flux densities in the various cameras/filters are listed in Table 4. The errors are of the order of 3–30% and, in the inner part of the jet, is likely dominated by the uncertainties related to the galaxy subtraction.

For optical non-detections, we quote 3σ upper limits. Furthermore, the flat-fielded images of ACS are characterized by a geometric distortion. For this reason we applied a field-dependent correction: Using the plot of the Pixel Area Map (PAM) reported at the *HST* webpage www.stsci.edu/hst/acs/analysis/PAMS for the WFC1 channel of the ACS, we found that the coefficient that has to be applied for the observation of 3C 371 is close to 0.985; to correct a flux measured on the flat-fielded file it is necessary to multiply by the PAM value and divide by the exposure time.

In the NICMOS image, after subtracting the galaxy contribution, the jet axis of 3C 371 appears to coincide with one of the diffraction spikes produced by the intense light from the core. The inner part of the jet is completely overwhelmed by the spike emission and no reliable estimate of the inner knot flux is possible. Although the spikes span the entire image and their intensities change irregularly with the distance from the central PSF, we note that 1) opposite spikes are approximately symmetric, and 2) their intensities decrease dramatically at $\sim$3″ from the core. That is, it is possible to roughly estimate the emission in the outer part of the jet after removing the contamination due to the spike. To perform this task, from the NICMOS image we subtracted the image itself rotated by 180°. This estimate has to be used with caution since spurious fluctuations can remain due to uncertainties in the relative intensity of the diffraction spikes.

2.4. *Radio*

As part of our *Chandra*/*HST* imaging program of these jets, we obtained new deep radio observations of the tar-

gets supplemented by a number of archival data sets. The data processing was done with AIPS (Bridle & Greisen 1994) and DIFMAP (Shepherd et al. 1994) using standard procedures. Table 3 reports the log of the radio observations including archival data sets used for both sources.

The new 22 GHz observations were obtained with the NRAO Very Large Array (*VLA*) as part of our observing program on large-scale X-ray jets (Cheung 2004; Sambruna et al. 2006). Both objects were observed over a wide range of hour angles for uniform coverage of the (u, v) plane during separate observing runs – 3C 371 in the B-configuration and PKS 2201+044 with the hybrid AnB configuration to improve the north-south resolution for this lower declination source. The total integrations of $\sim$3 hrs, and the off-source rms is near the theoretical noise limit of $1\sigma\sim$0.1 mJy beam^{-1}.

Comparably high resolution ($\sim$0.25") radio maps at 1.4 GHz were obtained from *MERLIN* (Table 3). A new full-track observation of PKS 2201+044 was obtained and for 3C 371, we use the full resolution version of the data originally presented in P01.

To facilitate comparison with the largest scale structure (beyond knot A), we present 2.1″ resolution maps of 3C 371 at 5 GHz (from Wrobel & Lind 1990). Radio emission beyond knot A in PKS 2201+044 is not quite visible in the existing data though lower resolution images show much extended structure (Ulvestad & Johnston 1984). We therefore obtained new subarcsecond-resolution *VLA* data at 8.5 GHz for this object which details more of the extended radio tail.

Polarization Images. Additional polarization calibration of the 8.5 GHz *VLA* data for PKS 2201+044 (Figure 6) shows appreciable polarization structure in the jet. The jet is initially highly polarized ($\sim$15–20%) with an inferred magnetic field transverse to the jet. At the jet flaring point of about 2″, there is more complex polarization behavior. The observed polarization angle in the central portion of knot A is consistent with that observed at 5 GHz (Laurent-Muehleisen et al. 1993). The agreement is within $\sim10^\circ$ which implies a small rotation measure of $\lesssim 76$ rad m^{-2} corresponding to a negligible polarization angle correction in our 8.5 GHz image. The edges of the jet in these regions are very highly polarized. On the northern edge (fraction polarization $\sim$50%), the inferred magnetic field orientation is parallel to the jet surface. Toward the southern edge, the polarization is at the theoretical maximum for synchrotron radiation ($\sim$70%) with no obvious alignment of the B-field vectors and the jet direction. At the spine of the jet in this region, the polarization is lower ($\sim$6–9%), presumably from dilution because of the large beam size and cancellation from line-of-sight component of the magnetic field in the sheath layer.

The polarization behavior in 3C 371 (Figure 7) is similar to the case of PKS 2201+044. Our analysis of an archival *VLA* 5 GHz data for 3C 371 shows similarly, highly polarized edges in knot A ($\sim$30–40%) with inferred B-field vectors parallel to the jet surface. We ignored the small correction $+3^\circ$ in the polarization angle at this frequency implied by the low rotation measure in this region of the jet (Wrobel & Lind 1990). The other datasets did not detect appreciable polarization in the jet. In contrast to the PKS 2201+044 case, the B-field orientation in the 3C 371 jet spine is parallel to the jet and about 25% polarized. These data are consistent with the polarization map presented previously by O'Dea et al. (1988), and with the optical polarization image obtained with *HST* ACS by Perlman et al. (2006).

3. IMAGING AND SPATIAL ANALYSIS

The 0.3–8 keV images of 3C 371 and PKS 2201+044 are shown in Figures 1 and 3, and Figures 2 and 4, respectively. Also shown are the multiwavelength images of the jets. Below we discuss separately the X-ray data for the cores and the X-ray and multiwavelength observations of the inner and outer jets.

3.1. *The X-ray Cores*

Inspection of the ACIS-S images suggests the presence of diffuse X-ray emission around the cores of both sources. For a more quantitative analysis we extracted the radial profiles of the core region, using a series of concentric annuli centered on the core and extending up to 400″ on the ACIS CCD, with the jets excised. For the extraction procedure, see Donato et al. (2004). The jet and field point sources contributions were excluded from the extraction regions.

The profiles are shown in Figure 5. The core PSF fits well the inner parts ($\lesssim$ 8-10″) of the profiles, indicating the dominance of the core emission at such small radii (dashed line). Above 100″ from the core, the profiles die into the ACIS background (dotted horizontal lines). However, excess flux over the PSF is present at $\sim 10''$, most prominent in 3C 371. This feature suggests emission from a diffuse component, which we identify as ambient thermal gas. We thus fitted the excess flux with a β model, which describes the thermal emission from gas in hydrostatic equilibrium (Cavaliere & Fusco-Fermiano 1976).

The results of the fits to the radial profiles with the composite PSF + β + background model are reported in Table 5; the model components and their sum (solid line) are plotted over the data in Figure 5. The fitted core radii of the thermal component are 5″, or $\sim$5 kpc, and 17″, or 9 kpc, for 3C 371 and PKS 2201+044, respectively, consistent with the X-ray haloes of FRIs. The diffuse component is weakly detected in PKS 2201+044 ($\lesssim 3\sigma$) and only by fixing the β parameter at 0.67, typical of FRIs (Worrall & Birkinshaw 1994), does the fit converge.

We extracted the ACIS spectra of the diffuse emission in 3C 371, using `panda` extraction region between 10 and 30″. The background was chosen in a region on the same CCD free of serendipitae sources. A good fit ($\chi^2_r = 1.16/10$) of the background-subtracted spectrum is obtained with a combination of a thermal component at soft energies ($kT = 0.2^{+0.1}_{-0.2}$ keV, abundances fixed $Z = 0.2/Z_\odot$) and a power law at higher frequencies ($\Gamma = 0.8 \pm 0.5$). The latter is likely an instrumental feature: in fact, we detect a $\Gamma = 0.8$ in the *Chandra*, but not in the *XMM-Newton*, spectra of diffuse emission around other AGN (Lewis et al. 2007, in prep.). If true, it could represent the onset of the non-thermal emission from relativstic particles in the diffuse gas. The 0.3–8 keV observed flux of the diffuse thermal component in 3C 371 is $F_{0.3-8\ keV} = 5.1 \times 10^{-14}$ erg cm^{-2} s^{-1}.

3.2. *The Jets*

Figures 1 and 3 show a montage of the multiwavelength images of the inner parts ($\lesssim 4''$) of the 3C 371 and PKS 2201+044 jets, respectively. The images are arranged in order of decreasing wavelength from radio to X-rays; the higher-resolution radio countours from *MERLIN* are overlaid on each image.

The outer parts of the jets on larger scales are shown in Figures 2 and 4. The lower-resolution *VLA* data are shown (left), and the countours overlaid on the *Chandra* map (right). The outer jet sections extend beyond the *HST* fields, so no information is available from these data on their optical emission.

Concentrating on the inner jets, Figures 1 and 3 show that the radio jets are detected at higher frequencies. For 3C 371 we show the galaxy subtracted NICMOS image. As mentioned above, the inner parts of the jets are located below one of the PSF spikes; however, diffuse IR emission is clearly seen from the region around knot A.

In both sources, the jets share a similar overall multiwavelength morphology: while the radio-to-optical/UV jets morphologies track each other well, the X-ray emission is concentrated near the core, and fades toward the end of the jet. This multiwavelength morphology is very similar to what observed in general for FRIs (Worrall et al. 2001), where the dominant emission mechanism is synchrotron. However, although the cores are quite bright at X-rays in both sources (see § 4), the contamination of the core PSF wings to the X-ray emission from the inner X-ray jets is negligible due to the choice of the background extraction region.

To better quantify the jet properties we extracted profiles along the main jet axis (longitudinal profiles) and perpendicular to it (transverse profiles) at three wavelengths: radio (1.35 GHz for 3C 371 and 1.41 GHz for PKS 2201+044), optical (F555W), and X-rays (0.3–8 keV). For 3C 371, the optical images were convolved using *fgauss* in *FTOOLS* with elliptical Gaussian functions of 1 pixel (2 pixels for STIS), with final resolution $\sim 0.15''$ matched to the radio. For PKS 2201+044 the radio resolution is $0.25''$; thus, its *HST* images were convolved with a Gaussian function of 2 pixels to achieve matching resolution to the radio. For both sources, the ACIS images were rebinned by a factor of 0.2, yielding an image pixel size of $0.1''$, and smoothed with `csmooth` with a sigma of 1.5 pixels, with final resolution of $\sim 0.9''$. At this resolution, some of the closest knot pairs (e.g., β and B in 3C 371) will be blended. Another issue is that, while the FWHM of any point source in the field is close to $1''$, the sub-pixel imaging artificially forces each X-ray event to be confined to a $0.1''\times 0.1''$ pixel and many of these will lie outside the extraction region. This increased Poisson noise could produce spurious features, e.g., the double-peak structure in the longitudinal X-ray profile of PKS 2201+044 around knot A (Figure 9).

The longitudinal profiles are shown in Figures 8 and 9. In the radio and optical, the profiles were extracted by collapsing the flux of the jet onto a box $4''$-long and $0.15''$-wide for 3C 371 and $0.25''$ for PKS 2201+044. In the X-rays we used boxes $4''$-long and $1''$-wide. The transverse profiles (Figures 10 and 11) were extracted from boxes $3.5''$-long and $0.15''$-wide for 3C 371 and $0.25''$-wide for PKS 2201+044 for the optical and the radio. In the X-rays, boxes $0.5''$-wide were instead used, representing a compromise between matching the ACIS resolution and the need to separate the knot emission as much as possible. The boxes were placed across the jet at given distances from the core (see below and figure captions), and collapsing the flux onto the main axis of the box.

3.2.1. *3C 371*

The inner jet is shown in Figure 1 at the various wavelengths. We confirm our previous result (P01) that the radio/optical jet of 3C 371 emits at X-rays in the deeper *Chandra* image. In addition, we find faint X-ray emission from the outer jet, beyond feature A at $\gtrsim 4''$ (Figure 2).

From radio to IR/optical and UV, the jet emission appears concentrated in a few bright knots at $\sim 0.9''$ (knot α) and $1.3''$ (knot β), then fades somewhat around knot B at $1.8''$, and picks up again in the lobe near knot A. The X-ray emission has a broad shoulder in correspondence to knots β and B, beyond which it decreases.

At the higher angular resolution of *MERLIN* and *HST*, "knot" A is resolved into a more complex structure. Here, the emission is spread over a $\sim 1''$-long feature piled against the southeast intensity contours of the radio lobe. The radio and optical emission then declines gradually from the southern to the northern border of the emission region (knot A). The poorer *Chandra* resolution prevents a detailed mapping of the faint X-ray emission. Interestingly, the jet changes direction at this location (Figure 2). This strongly suggests that knot A is the site of an impact of the jet against some external dense medium, where shocked plasma emits optical and X-rays as a result of the compressed magnetic field and accelerated electrons.

The longitudinal profiles of the inner jet are shown in Figure 8. The extraction box was located at a position angle PA=55°; the four main radio/optical features are labelled (see Table 1). This Figure emphasizes the overall good correspondence between the radio and the optical, which peaks in correspondence of knot α and structure A; again, the X-ray profile fades downstream of knot B.

Emission profiles transverse to the jet axis taken at the position of knot B, structure A, and at an intermediate location ($2.4''$) between the two are shown in Figure 10. The main apparent feature is that the profiles are resolved at all three wavelengths. If the three X-ray profiles are approximated by Gaussians, the ensuing FWHMs are 1.0–$1.3''$. After deconvolving the $0.9''$ of the image PSF, the intrinsic region size for the resolved knot is 0.6–$0.9''$.

This extension is not an effect of the ACIS PSF. To illustrate this, using `CHART` and `MARX` we simulated the 37 ks ACIS observation of 3C 371 including the core and extended thermal emission in addition to the jet. The core and knots A and B were assumed to be point-like, while the thermal emission around the core was described by a beta-model (Cavaliere & Fusco-Fermiano 1976) with the observed characteristic radius of $5''$ and the β parameter fixed at 0.5 (see § 3.1). The observed ACIS-S spectra were used to model the various components (i.e., core and knots). Figure 12, top panels, shows the observed ACIS image (left) and the simulation overlaid with the observed X-ray contours (center). Note the larger X-ray contours compared to the simulated image; the excess flux of the

observation with respect to the the simulation is significant at P>99.99%. The transverse profiles of the observed and simulated knot A are compared in the top-right panel of Figure 12. Thus, we conclude that the large aspect ratio of the jet at X-rays is real and significant.

The only X-ray jet resolved so far orthogonally to its axis is in the close-by FRI Centaurus A, in a long (95 ks) *Chandra* ACIS-S exposure (Kataoka et al. 2006); it has a flat-topped profile suggestive of limb-brightening, previously observed at radio frequencies only (Giovannini et al. 2000). The opening angle of the jet in X-rays is half as large as at radio (Kataoka et al. 2006).

As apparent from Figure 7, the polarization images show the presence of a structured jet. There are two peaks in the linear polarization map separated by $\sim 1''$ in correspondence to knot A. Moreover, the magnetic field lines are denser toward the edges of the jet, indicating a "spine/wall" jet structure, which is also observed with *HST* (Perlman et al. 2006). This raises the possibility that the X-ray spectrum may be different at the jet center and periphery. We will investigate this issue in § 4.2.1 referring to the central and lateral parts of the jet as "spine" and "edges"; see Figure 13 and § 4.2.1 for their definition.

We turn now to the outermost part of the jet at $\gtrsim 4''$. Figure 2 shows how the radio jet changes direction after structure A, and has three knots of emission terminating in a diffuse lobe at $25''$ from the core. Interestingly, the first radio knot at $\sim 11.8''$ is weakly detected at the X-rays, while no high-energy emission is detected from the diffuse radio lobe or the counterlobe. For this radio knot we estimated a net count rate of $4\pm1 \times 10^{-4}$ c/s. Using `PIMMS` and assuming a spectral index $\Gamma = 2$, the evaluated unabsorbed flux at 0.3–8 keV is 2.3×10^{-15} erg cm^{-2} s^{-1} corresponding to a flux density at 1 keV of 0.3 nJy. No information is present in the optical, because of the smaller field of view of *HST*.

3.2.2. *PKS 2201+044*

Figure 3 shows the innermost portions of the jet in PKS 2201+044. In the radio, the jet emerges from the core as a narrow, collimated stream ending in a bright enhancement region at $1.1''$ (knot α). This is followed by another discrete emission region at $1.6''$ (knot β). Finally, the radio jet flares up again into a trident-like structure (A) at $2.2''$, consisting of three protruding elongations toward northwest.

In the optical, the emission from knots α and β is weak, while feature A is bright. The *Chandra* image shows faint and continuous X-ray emission from knot α to A. Indeed, there is little evidence of a well-defined peak of X-ray emission in the longitudinal profiles in Figure 9. Only an upper limit to the X-ray emission from α is reported in Table 1. The radio and optical peaks of knot α appear slightly offset from each other by $\sim 0.1''$–$0.2''$, a distance that is one order of magnitude greater than the *HST* differential astrometry. However, this could likely be an artifact due to galaxy subtraction, as well as the optical bump at $0.5''$ in Figure 9. After $3''$, the optical and X-ray emission decline rapidly into the background while at radio frequencies the intensity recovers into a smaller knot at $3.8''$. As mentioned in § 3.2, the double structure in the X-ray profile at knot A is probably an artifact of the rebinning procedure of the ACIS image.

Figure 11 shows the transverse profiles of the jet at $1.6''$ (knot β), $2.2''$ (knot A), and $2.8''$ (downstream). The knots are resolved at radio at optical but only marginally at X-ray wavelengths, with FWHMs $\simeq 1.1''$ at X-rays.

At $4''$ from the core the radio jet loses collimation, opening in a wide-cone wind with no discrete emission but rather a continuum, and changing direction around $5''$ (Figure 4). Diffuse X-ray emission is detected from the inner part of the wind and in particular in two regions located at $6.2''$ and $8.2''$ from the core. The extracted net count rates are $6\pm2\times10^{-4}$ c/s and $7\pm2\times10^{-4}$ c/s, for the two knots respectively. Also in this case we used `PIMMS` to derive the unabsorbed flux at 0.3–8 keV. Assuming a spectral index $\Gamma = 2$, we found that $F_{0.3-8\ keV} = 3.5 \times 10^{-15}$ erg cm^{-2} s^{-1} and $F_{0.3-8\ keV} = 4.1 \times 10^{-15}$ erg cm^{-2} s^{-1}.

3.2.3. *Inter-knot emission*

As is apparent from Figures 8 and 9, the emissivity at radio, optical, and X-rays does not go to zero in the regions between consecutive knots. The "dark" regions between the cores and first knots in the optical is an artifact due to the galaxy subtraction.

The presence of inter-knot emission is not new, having been noted previously in several FRII jets (Sambruna et al. 2006 and references therein). At X-rays, it is still not clear whether the inter-knot emission is truly continuous or due to unresolved discrete knots. Here we can only note that this emission is part of the "spine" of the jet. In § 4.2.1 we will investigate wheather spine and edges have different spectral properties at X-rays.

4. X-RAY SPECTRAL ANALYSIS

4.1. *The Cores*

Analysis of the core light curves show that the flux did not vary within the ACIS exposure of both sources. We thus concentrate on the total X-ray spectra, integrated over the entire ACIS exposures, and extracted as described in § 2.2.

The core spectra were fitted with a two-component model, both absorbed by Galactic $N_{\rm H}$, including a power law, to represent the AGN, and a thermal, to account for the circumnuclear thermal emission (§ 3.1). A component to account for the core pileup, albeit modest, was also included. The thermal component was parameterized by the model `apec` in `XSPEC`, with temperatures kT and elemental abundances $Z/Z_{\odot}$. During the initial fits we left the abundance free to vary from 0.2 and 1. The values of this parameter always pegged at one of the limits, thus we fixed the abundance at their best fit values, $Z/Z_{\odot}$=1 for PKS 2201+044 and 0.2 for 3C 371, to obtain more stringent constraints on the remaining parameters. For PKS 2201+044 the thermal component is not statistically significant ($P_F < 90\%$).

The results of the spectral fits are listed in Table 6, where the 0.3–8 keV total and power-law fluxes are listed separately. It can be inferred from the Table that, as expected from Figure 5, the thermal component contributes only 2–3% to the total X-ray emission of the core. The core spectrum is rather hard in both sources, $\Gamma \sim 1.5$, as in other BL Lacs of similar luminosity (e.g., Donato, Sambruna, & Gliozzi 2004).

4.2. *The inner jets*

4.2.1. *3C 371*

Spectra were extracted from knots β and B, and structure A following the procedure described in § 2.2. In all three cases, the 0.3–8 keV continua are adequately described by a single power law model with Galactic absorption, with the photon indices reported in Table 7. These indices are steeper than observed in FRIIs, and similar to those derived for FRIs (Worrall et al. 2003). The addition of a thermal component is not statistically significant, and a power law is preferred over a single thermal model.

Comparing with the photon index of the core, $\Gamma = 1.46$ (Table 6), it is clear that the X-ray continuum steepens going from the unresolved to the resolved jet. There is also a marginal trend of gradual softening of the X-ray emission along the jet, however, the uncertainties are too large to allow firmer conclusions. As discussed above, the core PSF contamination to the X-ray emission from knots β and B is negligible because of the choice of the extraction region for the background.

In § 3.2.1, evidence was presented that the X-ray jet is resolved transversally to its axis into a central region, or "spine", and lateral "edges". To quantify the X-ray properties of the "edge" emission, its ACIS spectrum was extracted. We used rectangular boxes of length $2.9''$ and width $0.9''$, located as illustrated in Figure 13, where the extraction region for the background is also shown. The X-ray spectra of the two edges were combined in order to increase the signal-to-noise ratio. Note that the background region includes an average of the circumnuclear thermal emission and the wings of the core PSF; these contributions are thus subtracted during the fits in `XSPEC`. We experimented with the position and size of the edges but found consistent spectral fits in all cases. We thus choose the case in Figure 13 because it corresponds to the highest signal-to-noise ratio.

Similarly, we extracted the X-ray spectrum of the central portion of the jet, labeled "spine" (Figure 13), using a rectangular region of dimensions $2.4''\times$ $1.3''$. The latter contains a total of ∼1,250 net counts in 0.3–8 keV; this includes the contribution of β, B, and A, but also the residual intra-knot X-ray emission. Because of the limited resolution and statistics, we make no attempt to remove the knot contributions to the spectrum.

Note that the extraction region for the "spine" is as wide as the entire X-ray jet; as such, the X-ray emission of both "spine" and "edges" is blended in the spine spectrum. On the other hand, the edge regions are sampling the wings of the flux distribution; because of the lateral extension of the X-ray jet, in the edge regions the "edges", if they have a different spectrum, will dominate the emission depending on the relative intensity of the two components. In summary, the relative contributions of the "spine" and "edges", while blended due to the intrinsic FWHM of ACIS, will differ in the two extraction regions.

A total of ∼260 net counts were extracted from the combined edges in 0.3–8 keV, sufficient for spectral analysis. A fit with a single power law and Galactic absorption yields a photon index $\Gamma_{edges} = 2.24^{+0.26}_{-0.25}$, $\chi^2_r = 0.91/13$, and an observed flux in 2–10 keV of $F_{edges} \sim 1.7\times10^{-14}$ erg cm^{-2} s^{-1}. However, the residuals of the single power law model show a small ($\sim 1\sigma$) flux excess in the energy range 0.8–1 keV; the inclusion of a thermal model with temperature $kT \sim 1$ keV, albeit statistically not significant ($\Delta\chi^2$=2.7 for 3 additional free parameters), indeed produces flatter residuals. The possibility of thermal emission along the edges is of particular interest for gas entrainment models (Tavecchio et al. 2006). Additionally, structure A is highly suggestive of an impact of the jet with external medium, and thermal emission of shocked gas would be expected in this case.

For the "spine", a fit with a power law yields $\Gamma_{spine} = 2.01 \pm 0.08$, $\chi^2_r = 0.74/52$, and 2–10 keV flux $F_{spine} \sim 1.1 \times 10^{-13}$ erg cm^{-2} s^{-1}. Comparing with the edges, there is a slight indication that the spine has a harder X-ray emission than the edges, although this is only a 1σ effect. Better data are needed to confirm this result.

To test this result, we used the simulations reported earlier. Using the same extraction regions as in Figure 13 we extracted the ACIS spectra of the spine and edges. Comparing the two spectra, the opposite effect is observed: the edges' spectrum is *flatter* than the spine, because clearly dominated by the larger PSF at higher energies. The difference in slope is still 1σ. We thus conclude that there is marginal evidence for a possible spectral difference at X-rays between the spine and the edges, which needs to be confirmed in the future in higher-quality data.

In summary, the X-ray continua of the jet knots, edges, and spine are well described by a single power law model. We find evidence that the X-ray emission of the jet is softer than the core.

4.2.2. *PKS 2201+044*

In the case of the discrete jet knots, X-ray spectra were extracted as described in § 2.2, and fitted with a single power law plus Galactic absorption model. In all cases the power law is an adequate description, with no need for extra (thermal) components. The photon indices are similar to those derived for 3C 371 (Table 7). There is a suggestion for the X-ray continuum of the core to be harder than the outer jet (see § 4.1 and Table 6).

Figure 13 shows the extraction regions used for the spine and edges of the jet, using similar regions as for 3C 371. A total of 380 and 44 counts, respectively, were collected. The 0.3–8 keV continuum of the spine is well fitted by a power law with $\Gamma_{spine} = 2.07 \pm 0.18$, yielding an observed 2–10 keV flux $F_{spine} \sim 3.3 \times 10^{-14}$ erg cm^{-2} s^{-1}; for the edges, we find $\Gamma_{edges} = 2.7 \pm 1.8$ and 2–10 keV flux $F_{edges} \sim 3.0 \times 10^{-15}$ erg cm^{-2} s^{-1}.

The conclusions are very similar to 3C 371. We find an indication that the X-ray continuum of the PKS 2201+044 jet softens from the core to the lobe. However, large uncertainties plague the measurements of the slopes, and longer *Chandra* observations are required to confirm the spectral gradient along and possibly across the jet.

4.3. *Jet Spectral Energy Distributions*

The X-ray fluxes of the jet knots were extracted from elliptical regions with axes in the range 0.4–$1.1''$, as discussed in § 2.2. Because of the higher angular resolution, the optical fluxes were extracted using squared regions of smaller sizes, except for knots A (§ 2.3). The extraction regions at optical and X-rays were centered on the radio

position of the features. The radio extraction regions were ellipses with axes in the range 0.25–0.4″, depending on the size of the knots, but with an area similar to that covered by the extraction regions at optical. Table 4 lists the multiwavelength flux densities for the jet features, while the SEDs are shown in Figures 14 and 15. The fluxes in the Table and Figures are corrected for absorption, aperture, and PSF wing contamination (§ 2.2).

The continuum energy indices are reported in Table 7. In the radio band the slopes were calculated by interpolating to the corresponding datapoints; the uncertainties reflect the errors on the fluxes. For the radio fluxes, the errors are 12% at 1.35 and 1.4 GHz, and 15% at 22.4 GHz. For the optical, the errors on the flux were derived by averaging the statistical fluctuations of the latter in regions surrounding the extraction region (§ 2.3). However, except for knots A which are the most distant from the cores, uncertainties associated with the choice of the extraction region are likely to affect the optical slopes. In 3C 371, the optical data of knot A clearly indicate a softening of the optical spectrum with respect to the radio. The X-ray slopes were derived from fits to the ACIS spectra of the individual knots with a power law model (§ 3.3).

Broad-band spectral indices were also calculated, from radio to optical (α_{ro}), optical to X-rays (α_{ox}), and radio to X-rays (α_{rx}). These indices are listed in Table 7. These values were calculated between 5 GHz (using the interpolated flux), 5550 Å, and 1 keV.

5. DISCUSSION

5.1. *Modeling the knots' SEDs*

The SEDs shown in Figure 15 and the spectral indices reported in Table 7 reveal some interesting features. The broad-band indices α_{ro} and α_{ox} are remarkably similar along the same jet (except for knots A) and between the two jets, as well as the X-ray slopes α_X; the latter, however, have relatively large errors. For all knots, the X-ray continuum is softer than at radio, and softer than the radio to X-ray spectral index; the exception are knots α for which the X-ray flux could not be measured. On the whole the SEDs of knots A, in both jets, suggest that the emission derives from a single synchrotron component following a power law from the radio to the optical band, peaking close to the optical wavelength range and softening between the optical and X-rays. The SEDs of knots B (3C 371) and β (PKS 2201+044) are qualitatively similar to knots A, but with emission peaks in or close to the X-ray range. The optical fluxes of knot B in 3C 371 seem to deviate from a smooth connection between the radio and X-ray range. However, we note that this knot has the lowest optical flux and the measurement may suffer from systematic uncertainties.

Thus, the radio-to-X-rays SEDs can be modeled as synchrotron emission from relativistic electrons with a power law energy distribution up to some energy E_b, above which the power law steepens, probably as an effect of radiative cooling suffered by the high-energy electrons. This scenario would be qualitatively consistent with E_b shifting down in energy with increasing distance from the core.

As an example we model the overall emission observed from knot A of 3C 371 (Figure 16); given the similarity of the SEDs, the modeling of the emission from the other knots involves very similar parameter. We assume that the SED is described by synchrotron emission from a broken power law electron energy distribution. The emitting volume, assuming a sphere with radius of 0.3″, is $V = 4\times10^{63}$ cm^3 (equivalent to 0.14 kpc^3), the magnetic field (assumed to be in equipartition with the electrons) is $B = 73$ μG, the Doppler factor is fixed to $\delta = 2$ and the electron normalization is $K = 1.5\times10^{-4}$ part/cm^3. The distribution extends from minimum Lorentz factor $\gamma_{\rm min} = 1$ to the maximum $\gamma_{\rm max} = 10^8$ and we assume that the break is located at the Lorentz factor $\gamma_{\rm br} = 3\times10^6$. The low-energy slope is $n_1 = 2.35$, while the high-energy slope has been fixed to $n_2 = 3.55$ (close to the value $n_2 = n_1 + 1$ expected if the break derives from radiative cooling of the high-energy electrons). Broken power-law distributions are commonly adopted to describe the multifrequency data in other FRI jets (see e.g., Birkinshaw et al. 2002, Hardcastle et al. 2002).

Even assuming equipartition between magnetic and particle energies, the model is not sufficiently constrained by the observed SEDs, thus several model parameters have been chosen plausibly but arbitrarily. In particular, we lack information on the low-energy end of the electron distribution, $\gamma_{\rm min}$, and on the value of the Doppler factor, δ, both entering in the determination of the equipartition magnetic field.

In order to explore the effect of a different parameter choice on the estimate of the basic physical quantities of the jet we use analytical expressions relating the observed radio spectrum to the physical parameters (e.g., Tavecchio et al. 2006). The results are reported in Figure 17, both for knots A of 3C 371 and PKS 2201+044.

For a given choice of the values of the Doppler factor δ and $\gamma_{\rm min}$, we calculate the values of the other parameters (B and K) from the condition of equipartition and the value of the observed radio flux. In turn, the value of the Doppler factor can be translated into a value of the bulk Lorentz factor of the flow, Γ, necessary to calculate the jet power, assuming a given viewing angle, θ.

In the plots we show the resulting value of the power carried by the jet[2] as a function of the Doppler factor, for various choices of minimum Lorentz factor ($\gamma_{\rm min} = 10, 100, 10^3$) and viewing angles. The latter assumes the following values: $\theta = 18°$, $15°$, $10°$, and $5°$ for 3C 371, for which the upper limit comes from the observed jet/counterjet ratio measured at VLBI scales (Gomez & Marscher 2000); θ=40°, 20°, 15°, 10°, and 5° for PKS 2201+044, whose upper limit is obtained assuming a correlation between the observed radio power of the core and the total power, expected from the relativistic boosting at the base of the jet, at low frequency (Giroletti et al. 2004). For both sources, for magnetic fields $B < 100$ μG, the derived power ranges from $P_{\rm j} = 10^{42}$ erg s^{-1} to $P_{\rm j} = 10^{45}$ erg s^{-1}, consistent with the power inferred for other FRI jets (e.g., Bicknell & Begelman 1996; Laing & Bridle 2004). Note that, for a given choice of θ there is a limited range of allowed values for δ: this fact translates into the limited range of the parameters covered by the lines in Figure 17. The contribution of Inverse Compton emission, both SSC and External, is negligible at these

[2] We use the expression of the jet power reported in Schwartz et al. (2006).

frequencies for all the choices of the parameters.

An interesting issue concerns the nature of the knots observed in the two sources. A careful inspection of the multifrequency maps of both sources suggests a difference between the inner knots (α, β, and B for 3C 371; α and β for PKS 2201+044) and knots A. While the first features show a compact morphology, knots A, instead, are resolved at all wavelengths. In the case of knot A of 3C 371, moreover, the emission is more concentrated on one side of the jet (see Figure 1). As already noted (Nilsson et al. 1997), the position of this knot coincides with the location of a moderate change in the direction of the jet, clearly visible from the maps in Figure 2. It is tempting to associate the strong emission from knot A with the presence of an internal shock induced into the supersonical flow by the bending experienced by the jet. On the other hand, the location of knot A in PKS 2201+044 is close to the point where the jet seems to loose collimation and the surface brightness starts to decline. In this sense, this knot shares some similarities with the "flaring points" frequently observed in FRI jets, thought to mark the recollimation shock(s) expected when the decreasing pressure of the expanding jet reaches the value of the external medium (e.g., the discussion in Laing & Bridle 2002).

5.2. *The jets of 3C 371 and PKS 2201+044 in a broader context*

This paper presented multiwavelength observations with *Chandra*, *HST*, and the *VLA* of the relativistic jets in the nearby radio galaxies 3C 371 and PKS 2201+044. While *Chandra* has discovered and studied many extragalactic jets in FRIs and FRIIs so far (a list is maintained at XJET Website[2]), the sources of this paper stand out because of their "intermediate" properties.

From the point of view of their cores, both sources are classified as BL Lacs based on the continuum variability and polarization. However, narrow and broad emission lines were at times detected from the cores leading to an earlier classification as N galaxy (3C 371) and Seyfert 1 (PKS 2201+044). In 3C 371, however, the [OIII] emission appears extended in a S-W direction toward a nearby companion galaxy (Stickel, Fried, & Kühr 1993). While the core-jet radio morphology resembles that of FRIIs, particularly in the case of 3C 371 which shows prominent lobes, the total radio power and optical magnitude of the hosts of 3C 371 and PKS 2201+044 are similar to other FRIs (Ledlow & Owen 1996).

The data presented here support the idea that 3C 371 and PKS 2201+044 are intermediate sources between FRIs and FRIIs. As in FRIs, the X-ray emission peaks closer to the nucleus while the longer wavelength emission brightens towards the end. The polarization structure shows prominent features at the so-called "flaring point" on a similar physical distance from the nucleus as in other FRIs (e.g., Laing & Bridle 2002). In fact, the properties of 3C 371 and PKS 2201+044 resemble those of PKS 0521–365, which also exhibits an X-ray jet (Birkinshaw, Worrall, & Hardcastle 2002). In the latter source, a knot of X-ray emission was detected in earlier *Chandra* observations at 2″ from the nucleus, while the radio jet is three times longer. As in the sources of this paper, PKS 0521–365 is classified as a BL Lac although narrow and broad optical lines were detected from the core (Danziger et al. 1979).

On the other hand, the X-ray jets are one-sided as in FRIIs, but, unlike in FRIIs, they appear to be less collimated and do not exhibit the typical hard X-ray spectra present in high-power radio sources. The jet powers are also lower than typically derived for FRIIs (Sambruna et al. 2004). This is in agreement with a unified scenario where the differences can be understood on a physical basis. The different radio morphologies could result from jet deceleration occurring within the galaxy (FRIs) or outside the galaxy (FRIIs). Moreover, if the deceleration mechanism is entrainment of external gas, the scale length for deceleration is related to the jet power, which naturally accounts for the correlation of radio power and morphology (Bicknell 1995; Tavecchio et al. 2006).

Based on the multiwavelength properties of the jets one would conclude that these three sources - 3C 371, PKS 2201+044, and PKS 0521–365 - are FRIs with favorable orientations of their jets, i.e., more beamed than classical FRIs. The presence of broad optical emission lines from at least one of their nuclei may question this hypothesis, as FRIs generally are inefficient at producing broad optical lines (Baum, Zirbel, & O'Dea 1995). On the other hand, in higher luminosity BL Lacs, usually associated with FRIs, low states of the non-thermal continuum often uncover broad emission lines (Pian et al. 2002; Vermeulen et al. 1995).

6. SUMMARY

In this paper we presented and discussed multiwavelength observations of the jets in the nearby radio galaxies 3C 371 and PKS 2201+044, acquired using *Chandra*, *HST*, *VLA*, and *MERLIN*. Our primary findings are:

- The morphology of the jets is similar, with the X-ray emission brightening close to the nucleus and fading thereafter. This is comparable with other FRIs detected with *Chandra*;
- The SEDs of the knots are consistent with a single emission component from radio to X-rays, interpreted as synchrotron. The X-ray continuum steepens from the core to the end of the jet;
- The knots are resolved in a direction perpendicular to the jet axis at radio, optical, and X-rays. Radio polarization images indicate the presence of an edge-spine structure in both jets;
- The derived jet power ranges from $P_{\rm j} = 10^{42}$ erg s^{-1} to $P_{\rm j} = 10^{45}$ erg s^{-1};
- Overall, the X-ray jets of 3C 371 and PKS 2201+044 exhibit intermediate properties between low- and high-power radio sources.

While the jet and circumnuclear properties are completely consistent with those of other FRIs studied with *Chandra*, the nuclear properties of 3C 371 and PKS 2201+044 are unusual, in showing narrow and broad optical lines. It is thus possible we are seeing these jets at closer angles than in classical FRIs.

[2] http://hea-www.harvard.edu/XJET/

Many thanks to the anonymous referee for constructive criticism and a generally supportive attitude. The *VLA* is a facility of the National Radio Astronomy Observatory is operated by Associated Universities, Inc. under a cooperative agreement with the National Science Foundation. *MERLIN* is a UK National Facility operated by the University of Manchester at Jodrell Bank Observatory on behalf of PPARC. We thank Dr. Anita Richards for performing the initial pipeline calibration of the *MERLIN* data. Based in part on observations made with the NASA/ESA Hubble Space Telescope, obtained from the data archive at the STScI. STScI is operated by the Association of Universities for Research in Astronomy, Inc. under NASA contract NAS 5-26555.

REFERENCES

Aharonian, F. A. 2002, MNRAS, 332, 215
Angel, J. R. P., & Stockman, H. S. 1980, ARA&A, 18, 321
Baum, S. A., Zirbel, E. L., & O'Dea, C. P. 1995, ApJ, 451, 88
Bicknell, G. V. 1995, ApJS, 101, 29
Bicknell, G. V., & Begelman, M. C. 1996, ApJ, 467, 597
Birkinshaw, M., Worrall, D. M., & Hardcastle, M. J. 2002, MNRAS, 335, 142
Bridle, A. H., & Greisen, E. W. 1994, AIPS Memo 87 (NRAO: Charlottesville)
Cavaliere, A., & Fusco-Femiano, R. 1976, A&A, 49, 137
Celotti, A., Ghisellini, G., & Chiaberge, M. 2001, MNRAS, 321, L1
Cheung, C. C. 2004, Ph.D. Thesis, Brandeis University
Danziger, I. J., Fosbury, R. A. E., Goss, W. M., & Ekers, R. D. 1979, MNRAS, 188, 415
Dermer, C., & Atoyan, A. 2002, ApJ, 568, L81
Donato, D., Sambruna, R. M., & Gliozzi, M. 2004, ApJ, 617, 915
Fanaroff, B. L., & Riley, J. M. 1974, MNRAS, 167, 31P
Gehrels, N. 1986, ApJ, 303, 336
Georganopoulos, M., & Kazanas, D. 2004, ApJ, 604, L81
Giovannini, G., Cotton, W. D., Feretti, L., Lara, L., & Venturi, T. 2000, AdSpR, 26, 693
Giroletti, M., Giovannini, G., Taylor, G. B., & Falomo, R. 2004, ApJ, 613, 752
Gomez, J. -L., & Marscher, A. P. 2000, ApJ, 530, 245
Hardcastle, M. J., Worrall, D. M., Birkinshaw, M., Laing, R. A., & Bridle, A. H., & 2002, MNRAS, 334, 182
Kataoka, J., Stawarz, L., Aharonian, F., Takahara, F., Ostrowski, M., & Edwards, P. G. 2006, ApJ, 641, 158
Kollgaard, R. I., Wardle, J. F. C., Roberts, D. H., & Gabuzda, D. C. 1992, AJ, 104, 1687
Kollgaard, R. I., Gabuzda, D. C., & Feigelson, E. D. 1996, ApJ, 460, 174
Laing R. A., & Bridle, A. H. 2002, MNRAS, 336, 1161
Laing R. A., & Bridle, A. H. 2004, MNRAS, 348, 1459
Laurent-Muehleisen, S. A., Kollgaard, R. I., Moellenbrock, G. A., & Feigelson, E. D. 1993, AJ, 106, 875
Ledlow, M. J., & Owen, F. N. 1996, AJ, 112, 9
Ly, C., De Young, D. S., & Bechtold, J. 2005, ApJ, 618, 609
Marshall, H. L., et al. 2005, ApJS, 156, 13
Miller, J. S. 1975, ApJ, 200, L55
Nilsson, K., Heidt, J., Pursimo, T., Sillanpaeae, A., Takalo, L. O., & Jaeger, K. 1997, ApJ, 484, L107
O'Dea, C. P., Barvainis, R., & Challis, P. M. 1988, AJ, 96, 435
Perlman, E. S., et al. 2006, ApJ, 651, 735
Pesce, J. E., Sambruna, R. M., Tavecchio, F., Maraschi, L., Cheung, C. C., Urry, C. M., & Scarpa, R. 2001, ApJ, 556, L79 (P01)
Pian, E., et al. 2002, A&A, 392, 407
Sambruna, R. M., Maraschi, L., Tavecchio, F., Urry, C. M., Cheung, C. C., Chartas, G., Scarpa, R., & Gambill, J. K. 2002, ApJ, 571, 206
Sambruna, R. M., Gambill, J. K., Maraschi, L., Tavecchio, F., Cerutti, R., Cheung, C. C., Urry, C. M., & Chartas, G. 2004, ApJ, 608, 698
Sambruna, R. M., Gliozzi, M., Donato, D., Maraschi, L., Tavecchio, F., Cheung, C. C., Urry, C. M., & Wardle, J. F. C. 2006, ApJ, 641, 717
Sambruna, R.M., Donato, D., Cheung, C.C., Tavecchio, L., & Maraschi, L. 2007, in Proceedings of "Extragalactic Jets: Theory and Observation from Radio to Gamma Ray" ASP Conference Series, Eds. T. A. Rector and D. S. De Young (arXiv:0707.1321)
Scarpa, R., Urry, C. M., Falomo, R., & Treves, A. 1999, ApJ, 526, 643
Schlegel, D. J., Finkbeiner, D. P., & Davis, M. 1998, ApJ, 500, 525
Schwartz, D. A., et al. 2006, ApJ, 640, 592
Shepherd, M. C., Pearson, T. J., & Taylor, G. B. 1994, BAAS, 26, 987
Spergel, D. N., et al. 2003, ApJS, 148, 175
Stawarz, L., Sikora, M., Ostrowski, M., & Begelman, M. C. 2004, ApJ, 608, 95
Stickel, M., Fried, W., & Kühr, H. 1993, A&AS, 98, 393
Tavecchio, F., Maraschi, L., Sambruna, R. M., & Urry, C. M. 2000, ApJ, 544, L23
Tavecchio, F., Maraschi, L., Sambruna, R. M., Gliozzi, M., Cheung, C. C., Wardle, J. F. C., & Urry, C. M. 2006, ApJ ,641, 732
Uchiyama, Y., et al. 2006, ApJ, 648, 910
Ulvestad, J. S., & Johnston, K. J. 1984, AJ, 89, 189
Urry, C. M., Scarpa, R., O'Dowd, M., Falomo, R., Pesce, J. E., & Treves, A. 2000, ApJ, 532, 816
Vermeulen, R. C., et al. 1995, ApJ, 452, L5
Veron-Cetty, M. -P., & Veron, P. 1993, A&AS, 100, 521
Wardle, J. F. C., Moore, R. L., & Angel, J. R. P. 1984, ApJ, 279, 93
Worrall, D. M., & Birkinshaw, M. 1994, ApJ, 427, 134
Worrall, D. M., Birkinshaw, M., & Hardcastle, M. J. 2001, MNRAS, 326, L7
Worrall, D. M., Birkinshaw, M., & Hardcastle, M. J. 2003, MNRAS, 343, L73
Wrobel, J. M., & Lind, K. R. 1990, ApJ, 348, 135

TABLE 1
OBSERVED PROPERTIES OF X-RAY JET KNOTS

Knot (1)	Distance (2)	Counts Rate (3)	Backg (4)	$F_{1\ keV}$ (5)	$F_{0.3-8keV}$ (6)
		3C 371			
α	0.8	<32.2	···	<66.23	<80.12
β	1.3	6.2±0.4	1.1	9.23	7.35
B	1.9	5.9±0.4	0.4	12.98	10.26
A	3.1	2.4±0.3	0.1	6.98	4.82
		PKS 2201+044			
α	1.1	<29.7	···	<79.20	<81.18
β	1.6	1.8±0.3	0.5	3.77	3.10
A	2.2	2.0±0.2	0.1	5.63	4.21

Note. — **Columns explanation**: 1=Knot name; 2=Distance from the core (in arcsec); 3=Net count rate in the 0.3–8 keV band in units of 10^{-3} c/s; 4=Background count rate rescaled to the knot extraction region size in the 0.3–8 keV band in units of 10^{-3} c/s; 5=X-ray flux density at 1 keV (in nJy); 6=X-ray flux in the 0.3–8 keV band in units of 10^{-14} erg cm^{-2} s^{-1}. Fluxes and flux densities are aperture-corrected, background subtracted, and corrected for the contamination of the PSF wings of nearby knots. The total correction factors are 1.6, 2.3, and 2.7 for knots β, B, and A of 3C 371; and 2.2 and 2.9 for knots β and A of PKS 2201+044. The upper limits are 3σ above the surrounding background.

TABLE 2
HST OBSERVATION LOG

Instrument (1)	Aperture (2)	Filter (3)	Wavelength (4)	Obs. Date (5)	Exp. Time (6)
		3C 371			
NICMOS	NIC2-FIX	F160W	16030	1997-06-01	1152
WFPC2	PC1-FIX	F702W	6917	1994-08-18	560
ACS	WFC1-2K	F606W	5918	2003-09-20	658
WFPC2	PC1	F555W	5443	2001-06-23	3640
STIS	F25QTZ	MIRNUV	2357	2000-09-21	7989
		PKS 2201+044			
WFPC2	PC1-FIX	F702W	6917	1998-12-13	610
WFPC2	PC1	F555W	5443	2001-07-16	4240
STIS	F28X50LP	MIRVIS	7218	2001-07-16	2536

Note. — **Columns explanation**: 1=Instrument; 2=Aperture; 3=Filter; 4=Pivot wavelength (Å); 5=Observation date (yyyy-mm-dd); 6=Calculated total exposure time (s).

TABLE 3
RADIO OBSERVATION LOG

Telescope (1)	Obs. Date (2)	Frequency (3)	Exp. Time (4)	Resolution (5)	Program (6)	Obs./Ref. (7)
			3C 371			
MERLIN	1998 Apr 1/2	1.35	18	0.177x0.149	–	(1)
VLA	1986 Mar 21	4.86	0.79	0.804x0.387	AC150	(2)
	1985 May 05	4.99		2.1x2.1	–	(3)
	2002 Jul 21/22	22.46	3.31	0.2x0.2	AC641	(4)
			PKS 2201+044			
MERLIN	2000 Dec 21	1.41	11	0.336x0.169	MN/01A/04	(4)
VLA	2002 Jun 06	8.46	1.99	0.75x0.75	AC641	(4)
	2002 May 28	22.46	3.3	0.252x0.124	AC641	(4)

Note. — **Columns explanation**: 1=Telescope; 2=Observation Date; 3=Frequency (in GHz); 4=Exposure Time (in hours); 5=Resolution (in arcsec); 6=Program Code; 7=Observer or Published reference: (1)=Pesce et al. (2001); (2)=J. Conway; (3)=Wrobel & Lind (1990); (4)=C.C. Cheung.

TABLE 4
MULTIWAVELENGTH FLUXES

3C 371

Knot (1)	Distance (2)	$F_{1\ keV}$ (3)	$F_{2358\ \mathring{A}}$ (4)	$F_{5443\ \mathring{A}}$ (5)	$F_{5918\ \mathring{A}}$ (6)	$F_{22.46\ GHz}$ (7)	$F_{1.35\ GHz}$ (8)
α	0.9	<66.2	1.4	2.2	2.7	2.5	18.1
β	1.3	9.2	0.7	0.8	1.0	1.1	9.4
B	1.8	13.0	0.4	0.5	0.5	1.3	9.7
A[a]	3.1	7.0	1.8	3.6	4.4	4.5	31.7

PKS 2201+044

Knot (1)	Distance (2)	$F_{1\ keV}$ (3)	$F_{5443\ \mathring{A}}$ (4)	$F_{6917\ \mathring{A}}$ (5)	$F_{7219\ \mathring{A}}$ (6)	$F_{22.46\ GHz}$ (7)	$F_{1.41\ GHz}$ (8)
α	1.1	<79.2	0.6	<1.1	1.0	0.9	6.9
β	1.6	3.8	0.8	<1.1	1.0	1.0	4.9
A	2.2	5.6	3.5	4.7	4.6	2.6	18.7

Note. — **Columns explanation**: 1=Knot name; 2=Distance from the core (in arcsec); 3=X-ray flux density at 1 keV (in nJy); 4-6=Optical flux densities at the indicated wavelengths (in μJy). X-ray and optical fluxes are absorption- and aperture-corrected. The upper limits are 3σ; 7-8=Radio flux densities at the indicated frequencies (in mJy).

[a]This feature was also detected by NICMOS at λ = 16030 Å, with $F_{16030\ \mathring{A}} = 9.5\mu$Jy after galaxy and diffraction spike subtraction, and correcting for aperture.

TABLE 5
CORE RADIAL PROFILES

	3C 371	PKS 2201+044
r_c	$5.05^{+5.68}_{-5.05}$	17.38±7.35
β	0.42±0.08	0.67 fix
Norm.	$1.81^{+1.90}_{-1.81}$	0.37±0.22
χ^2_r/d.o.f.	1.98/101	1.61/102
P_F	>99.99%	99.1%

Note. — Results of the spatial analysis of the radial profile around the cores of 3C 371 and PKS 2201+044. We report the core radius (in arcsec), β, and normalization (in units of 10^{-5} counts s^{-1} $arcsec^{-2}$) of the β model, the reduced χ^2 and degrees of freedom, and F-test probability P_F for the addition of the β model to the fit.

TABLE 6
CORE SPECTRAL FITS

		3C 371	PKS 2201+044
Thermal	kT	0.29±0.04	
	Z	0.2 fix	
Power law	Γ	1.46±0.06	1.59±0.04
χ^2_r/d.o.f.		0.94/176	1.02/110
Total Flux		3.4	
Total Lum.		20.1	
P.law Flux		3.3	1.41
P.law Lum.		19.6	2.61

Note. — Results of the spectral analysis of the cores of 3C 371 and PKS 2201+044. The temperature is in keV and the abundance Z is with respect to solar values, $Z/Z_\odot$. The observed fluxes and intrinsic (absorption-corrected) luminosities are in the energy range 0.3–8 keV and in units of 10^{-12} erg cm^{-2} s^{-1} and 10^{42} erg s^{-1}, respectively.

TABLE 7
JET SPECTRAL INDICES

Source	Knot	α_{rx}	α_{ro}	α_{ox}	α_R	α_O	α_X
3C 371	α	>0.66	0.70	>0.58	0.70±0.07	0.74 ± 0.17	···
	β	0.73	0.72	0.74	0.76±0.07	0.39 ± 0.25	0.9 ± 0.3
	B	0.71	0.77	0.60	0.73±0.07	0.19 ± 0.39	1.0 ± 0.2
	A	0.82	0.70	1.03	0.69 ± 0.07	0.92 ± 0.08	1.1 ± 0.4
PKS 2201+044	α	>0.59	>0.73	>0.32	0.75±0.07	1.93 ± 1.40	···
	β	0.75	>0.69	>0.88	0.59±0.07	1.08 ± 1.20	0.9 ± 0.5
	A	0.80	0.66	1.06	0.71 ± 0.07	0.97 ± 0.20	1.1 ± 0.4

Note. — The broad-band indices were calculated using the monochromatic fluxes at 5 GHz, 5550Å, and 1 keV (see text and Table 4).

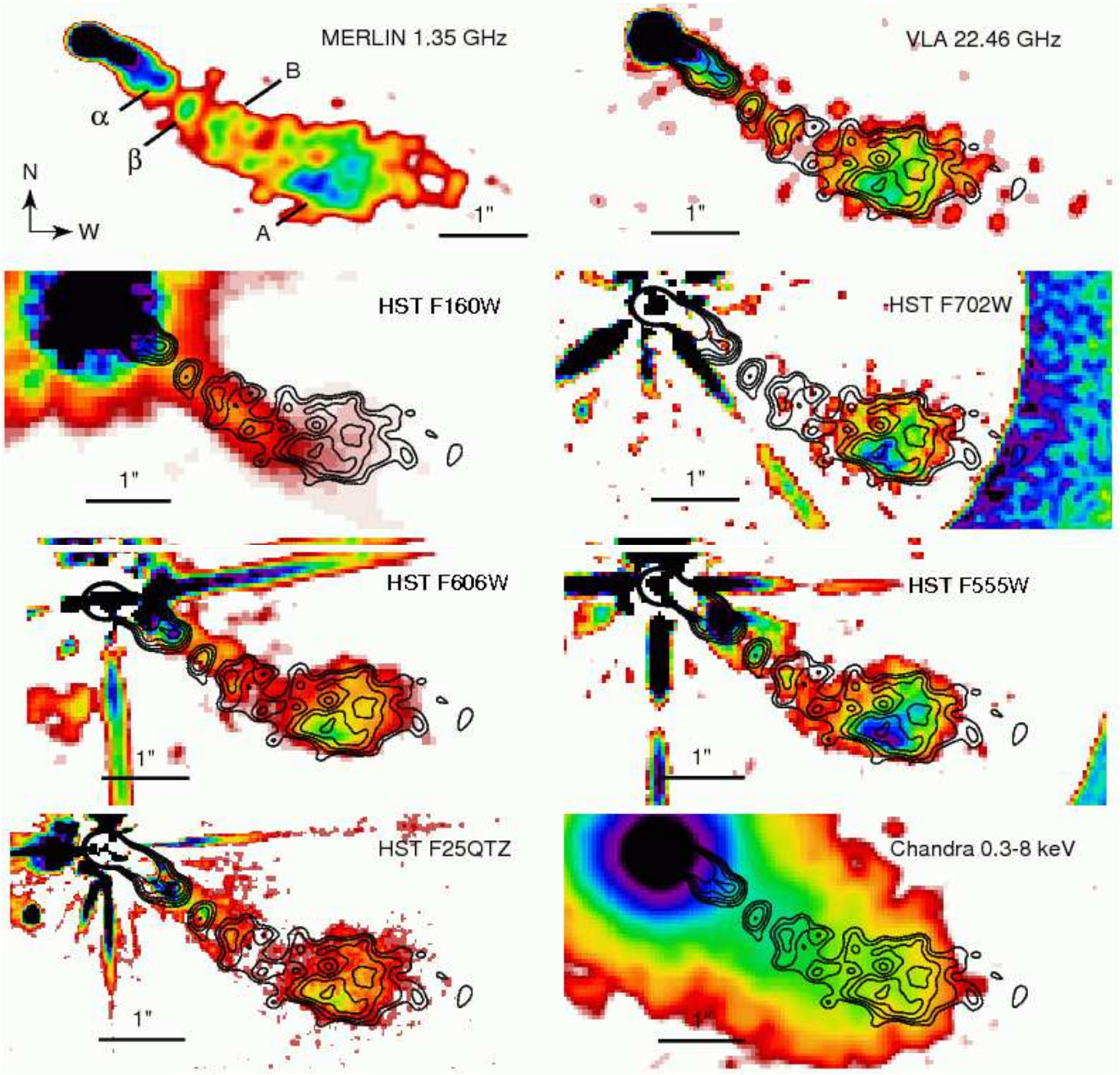

FIG. 1.— Images of the inner part of the jet of 3C 371 at the various wavelengths. First row: *MERLIN* (1.35 GHz) and *VLA* (22.46 GHz); Second row: NICMOS (F160W) and WFPC2 (F702W); Third row: ACS (F606W) and WFPC2 (F555W); Fourth row: STIS (F25QTZ-NUV-MAMA) and *Chandra* 0.3–8 keV. The radio images have a resolution of $\sim 0.18 \times 0.15''$ and $0.2''$, respectively. The optical images have been convolved using *fgauss* in *FTOOLS* with elliptical Gaussian function of 1 pixel (2 pixels for STIS), with final resolution $\sim 0.15''$. In the NICMOS image, the inner part of the jet is buried under a diffraction spike (see text). The X-ray image has been rebinned by a factor of 5 (final image pixel of $0.1''$) and then smoothed with the *csmooth* in *CIAO* with a circular Gaussian of $0.1''$, with final resolution $0.9''$ FWHM. In all cases, the 1.35 GHz radio contours are overlaid on the color image.

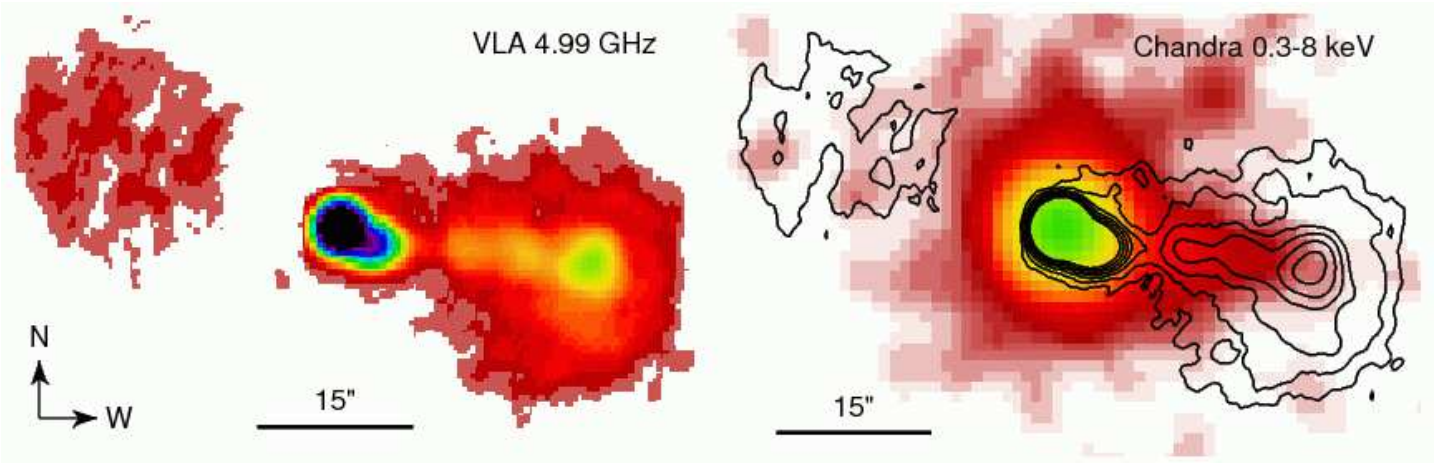

FIG. 2.— Images of the outer part of the jet of 3C 371. Left: *VLA* (5 GHz); Right: *Chandra* 0.3–8 keV. The radio image has a resolution of 2.1″. The X-ray image was rebinned by a factor of 2 (final image pixel of 1″) and smoothed with a circular Gaussian of 2″.

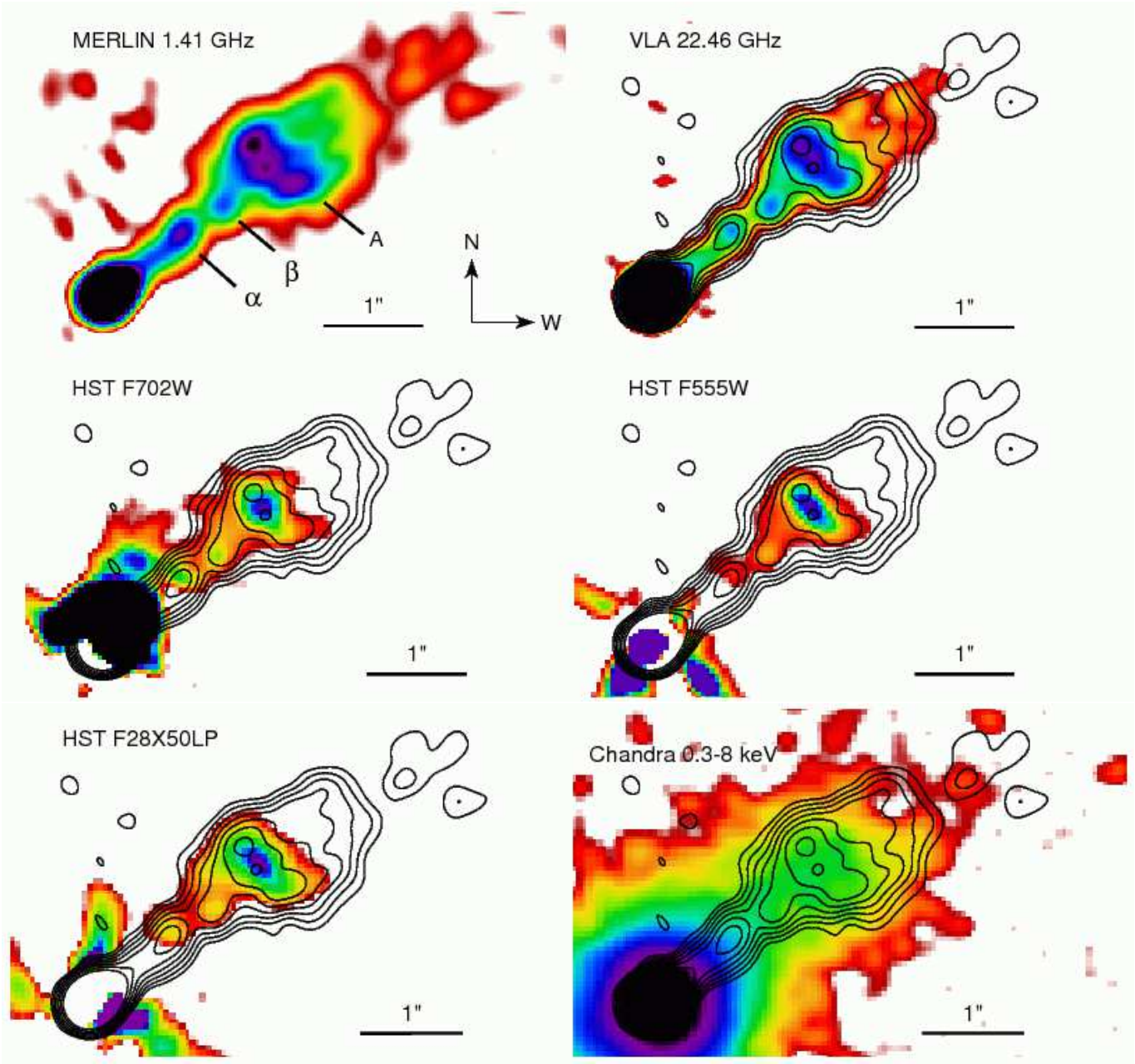

FIG. 3.— Images of the inner part of the jet of PKS 2201+044. First row: *MERLIN* (1.41 GHz) and *VLA* (22.46 GHz); Second row: WFPC2 (F702W and F555W); Third row: STIS (Broadband F28X50LP) and *Chandra* 0.3–8 keV. The radio images have a resolution of 0.25″. The optical and X-ray images have been obtained using the same procedure adopted for 3C 371 (see Figure 1). The 1.41 GHz radio contours are overlaid on all color images.

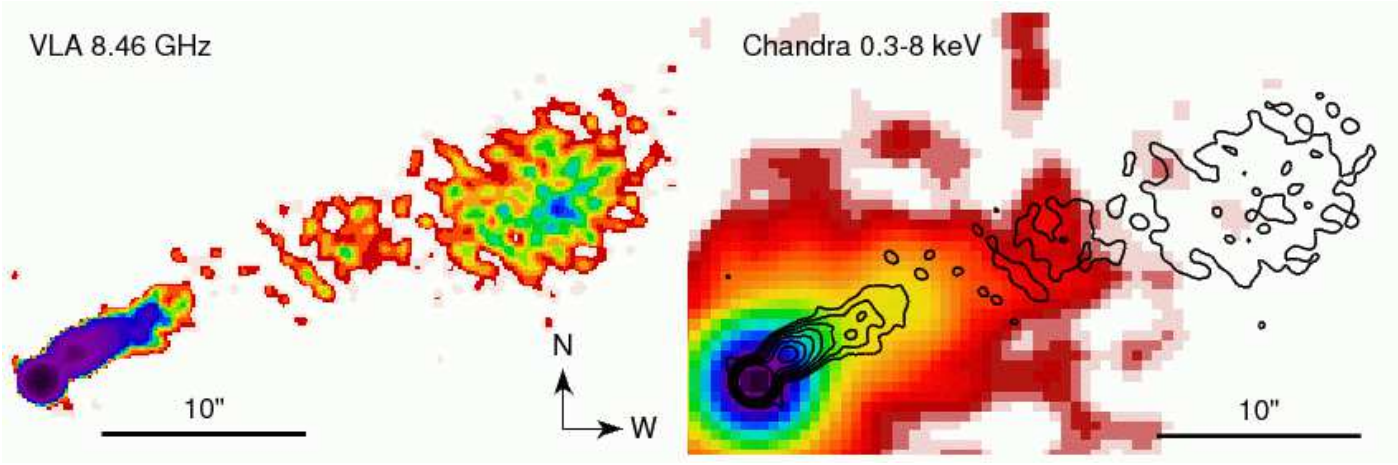

FIG. 4.— Images of the outer part of the jet in PKS 2201+044. Left: *VLA* (8.46 GHz); Right: *Chandra* 0.3–8 keV. The radio image has a resolution of 0.75″. The X-ray image was smoothed with a circular Gaussian of 1″.

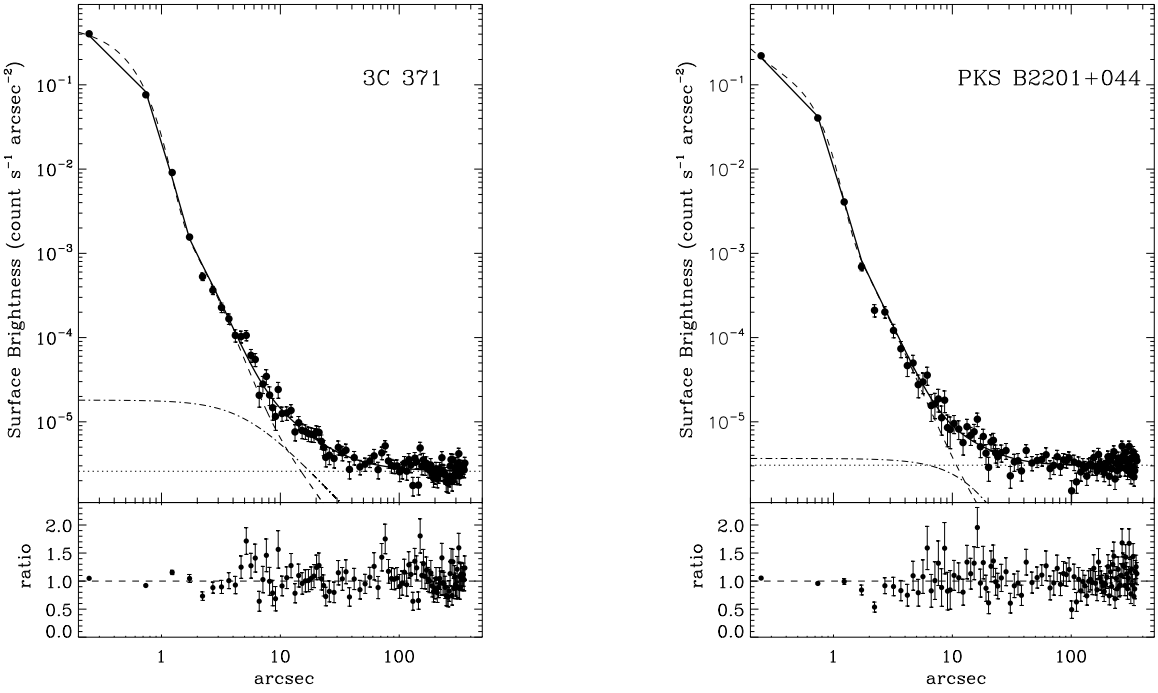

FIG. 5.— X-ray (0.3-8 keV) radial profiles of the two sources. In the top panels, the dashed line represents the instrumental PSF, and the dot-dashed line the β-model describing the diffuse emission. The continuous thick line is the total model, while the thin dotted horizontal line is the background. The residuals of the best-fit model are shown in the bottom panels.

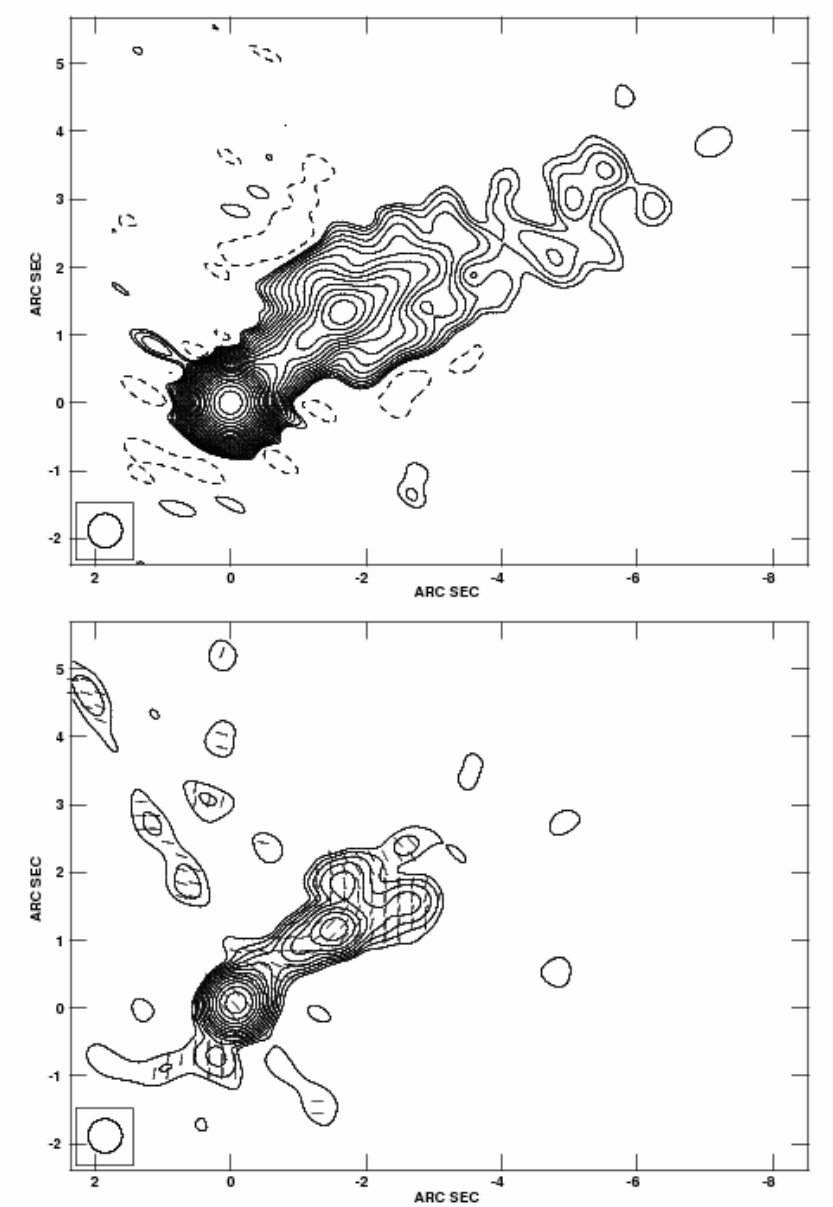

FIG. 6.— *VLA* total intensity [I; top] and polarization [P; bottom] images of PKS 2201+044 at 8.5 GHz. The short solid lines in the bottom panel represent the observed electric field. Contour levels begin at 0.11 (I) and 0.125 (P) mJy/bm and increase by factors of $\sqrt{2}$ to peaks of 306.5 (I) and 7.2 (P) mJy/bm. The images are "super-resolved" with a 0.5″ beam which is ∼1/2 of the naturally weighted beam.

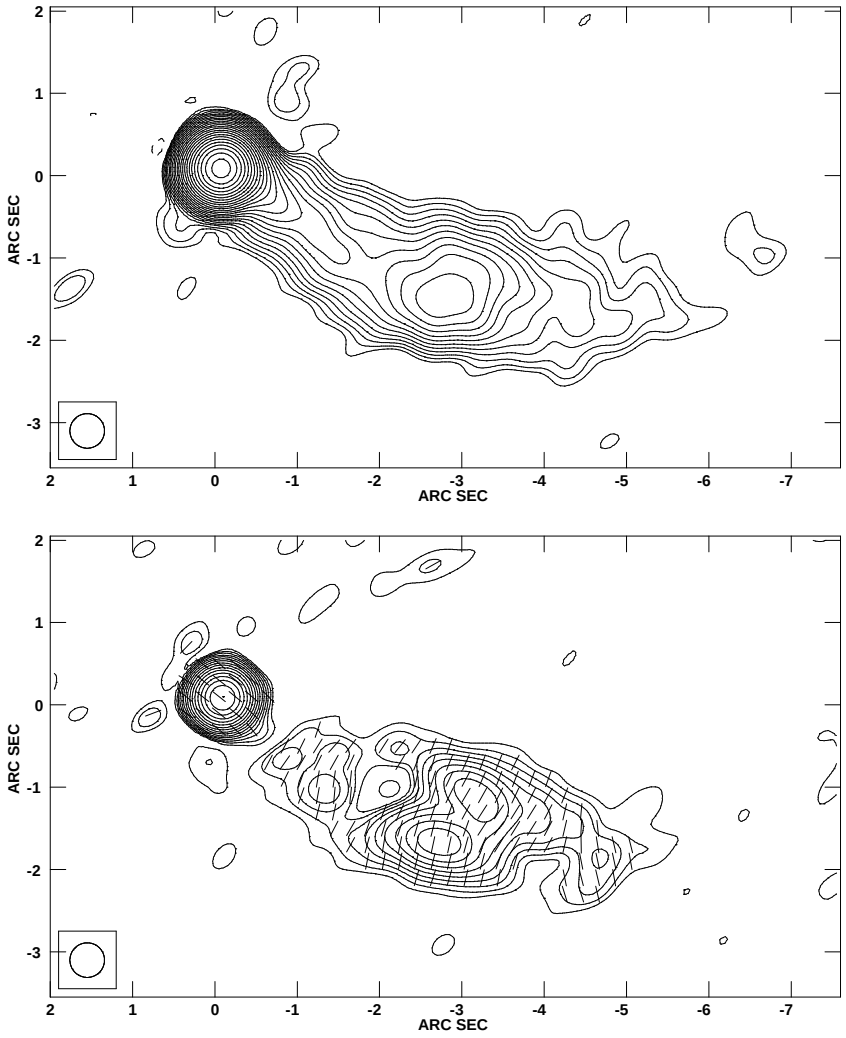

FIG. 7.— *VLA* total intensity [I; top] and polarization [P; bottom] images of 3C371 at 5 GHz. The short solid lines in the bottom panel represent the observed electric field. The contour levels begin at 0.45 (I) and 0.25 (P) mJy/bm and increase by factors of $\sqrt{2}$ to peaks of 1577.5 (I) and 45.3 (P) mJy/bm. The restoring beam of 0.42 arcsec is plotted on the bottom left of each panel. The tick marks indicate the orientation of the observed electric vector position angles.

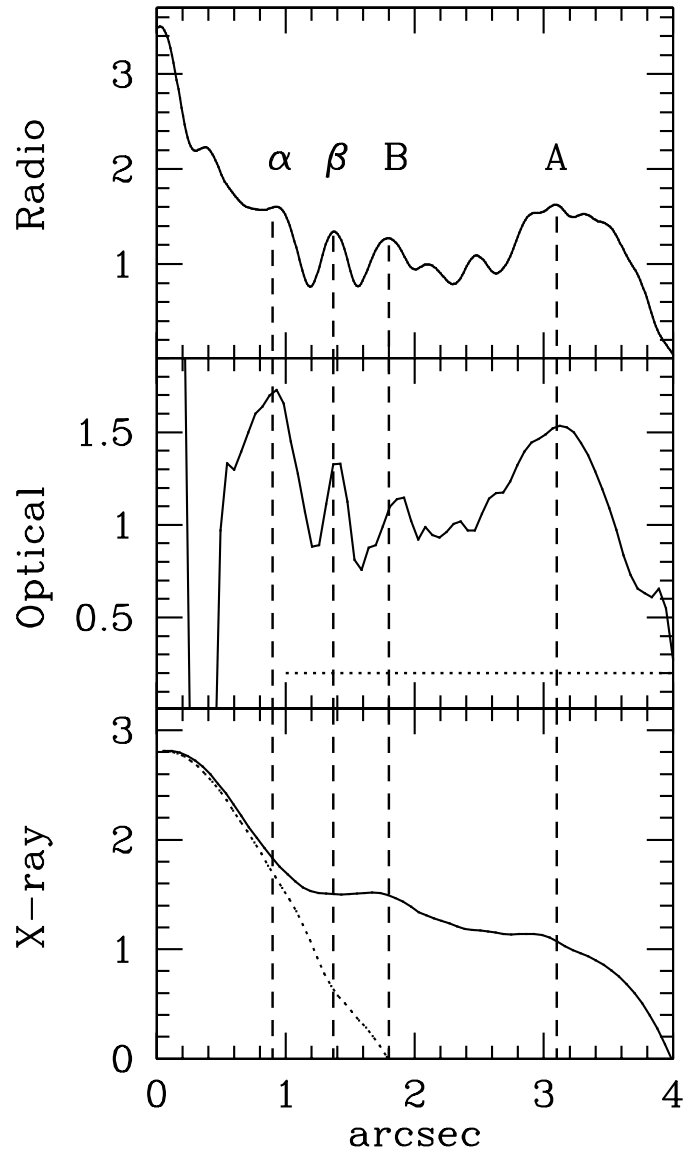

FIG. 8.— Longitudinal profiles at three wavelengths for the jet of 3C 371: Radio at 1.35 GHz, optical at 5443 Å, and X-ray in the 0.3-8 keV range (see § 3.2 for the technical description of the images). The units of the y-axis, in logaritmic scale, are Jy/beam at radio, and counts/pixel at optical and X-ray. The dashed line in the central panel marks the optical background. The radio and X-ray backgrounds (including the thermal emission in the latter) are off scale, more than one order of magnitude lower than the jet emission. Also shown in the X-ray profile is the profile at an azimuth of 180° from the jet. The lack of data around 0.4″ in the optical profile is an artifact due to the galaxy subtraction. The uncertainties on the fluxes are of the order of 5–30% for the X-rays, 3–30% for the optical, and 12–15% for the radio.

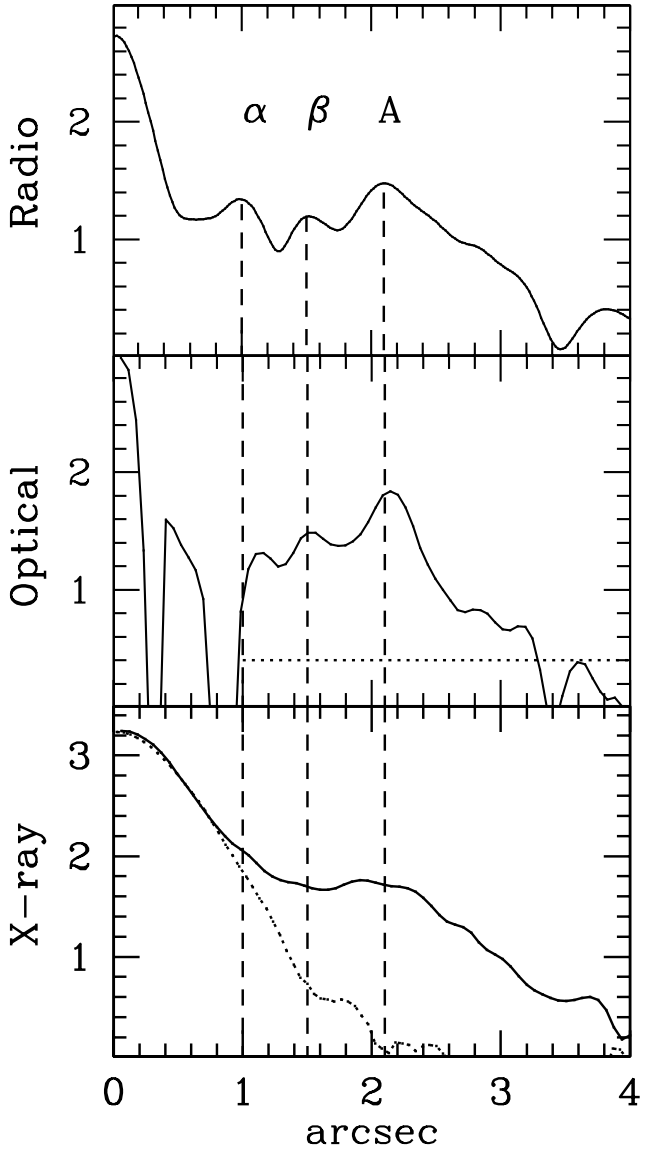

FIG. 9.— Longitudinal profiles at three wavelengths for the jet of PKS 2201+044: Radio at 1.41 GHz, optical at 5443 Å, and X-ray in the 0.3-8 keV range (see comments of Figure 8). Also shown in the X-ray profile is the profile at an azimuth of 180° from the jet. The lack of data around 0.3″ and 0.9″ in the optical profile is an artifact due to the galaxy subtraction. Uncertainties as for Figure 8.

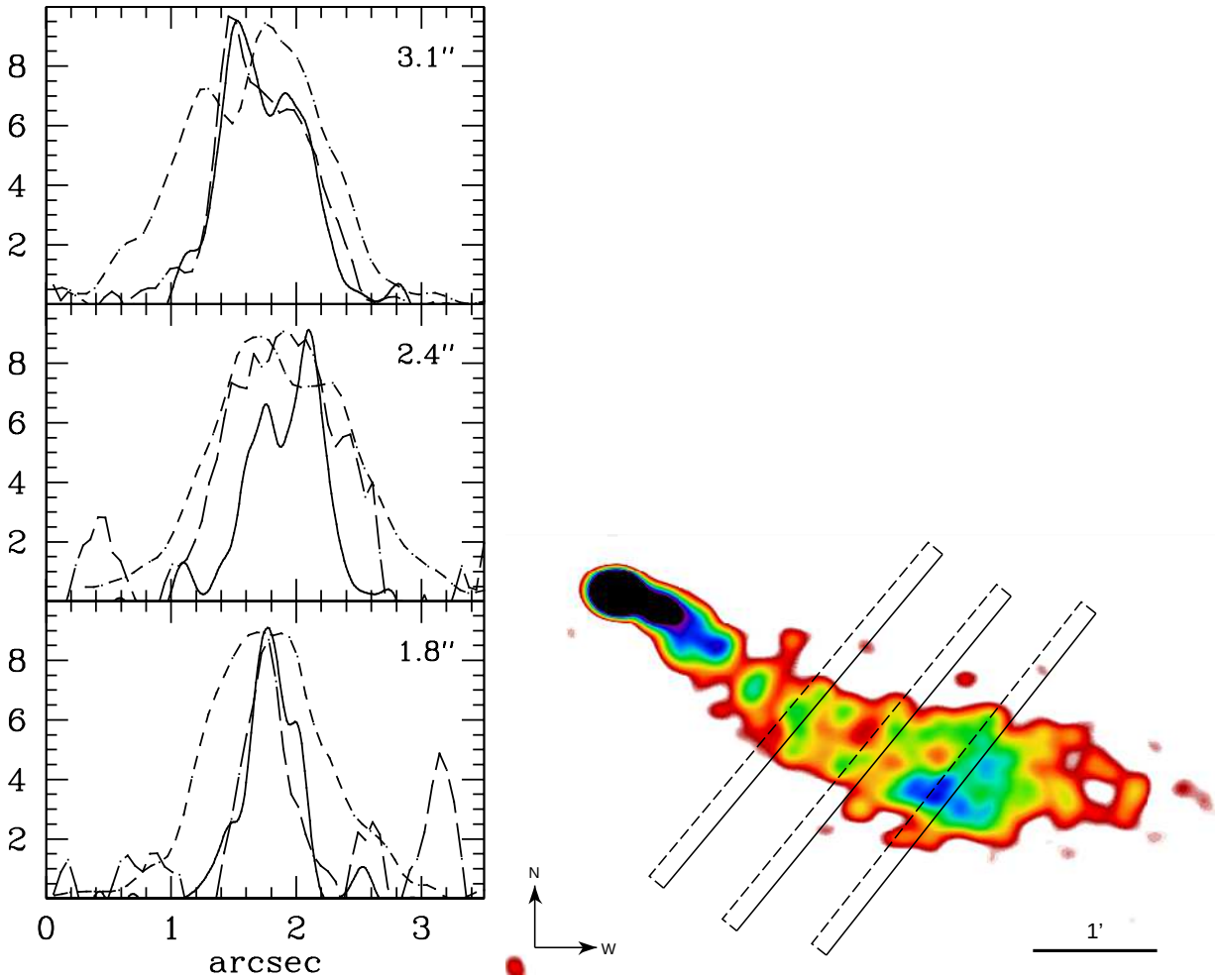

FIG. 10.— Normalized transverse profiles at three wavelengths for the jet of 3C 371 at a distance 3.1″ (knot A, top), 2.4″ (center), and 1.8″ (knot B, bottom). In all panels, the y-axis is expressed in arbitrary units, the solid line is the radio, the long-dashed line the optical, and the short-dashed line the X-rays. The profiles are extrated from the same images used for the profiles in Figure 8. Also shown in the companion panel are the positions of the extraction regions on the radio image. Uncertainties as for Figure 8.

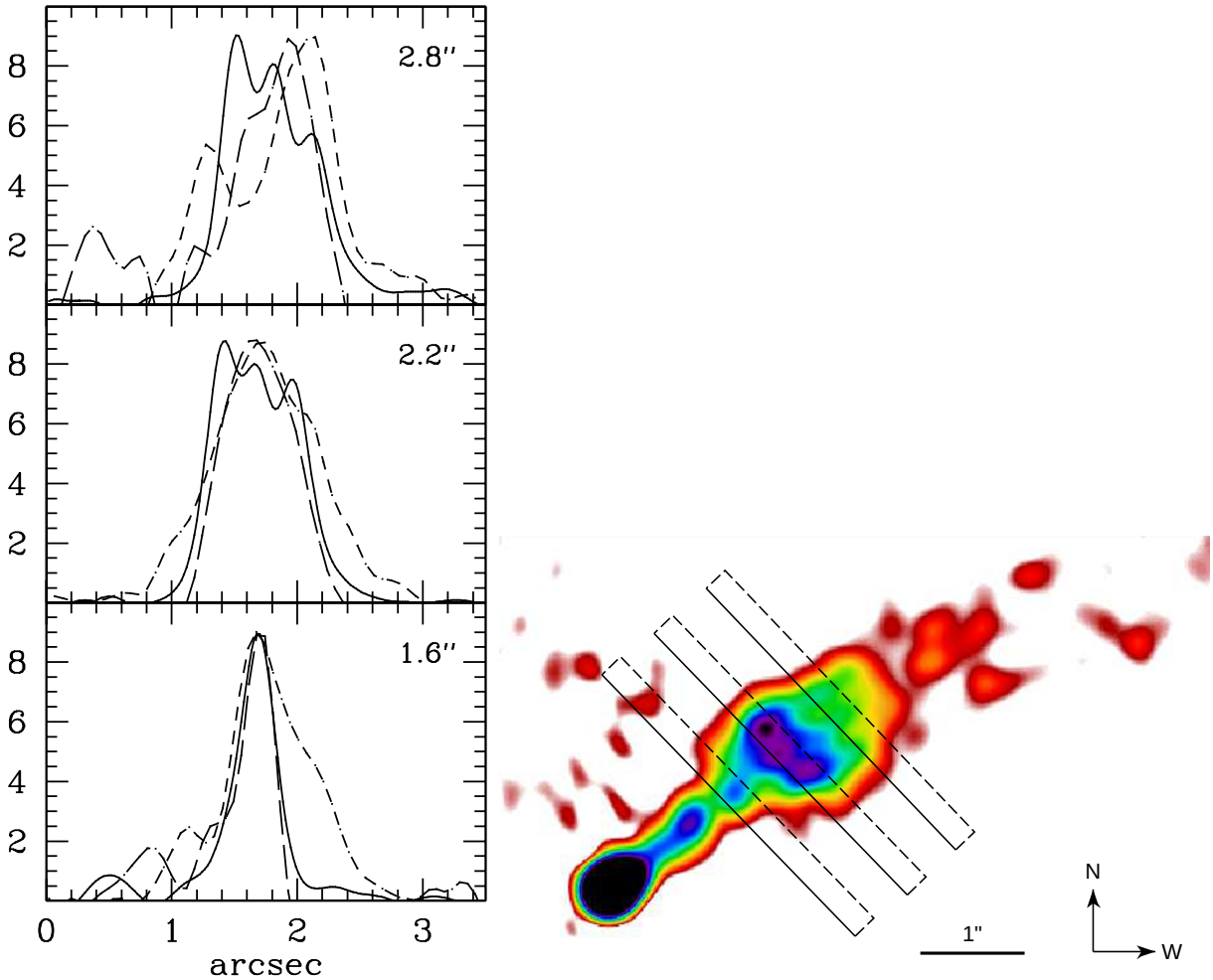

FIG. 11.— Normalized transverse profiles at three wavelengths for the jet of PKS 2201+044 at a distance 2.8″ (top), 2.2″ (knot A, center), and 1.6″ (knot β, bottom). In all panels, the y-axis is expressed in arbitrary units, the solid line is the radio, the long-dashed line the optical, and the short-dashed line the X-rays. The profiles are extrated from the same images used for the profiles in Figure 9. Also shown in the companion panel are the positions of the extraction regions on the radio image. Uncertainties as for Figure 8.

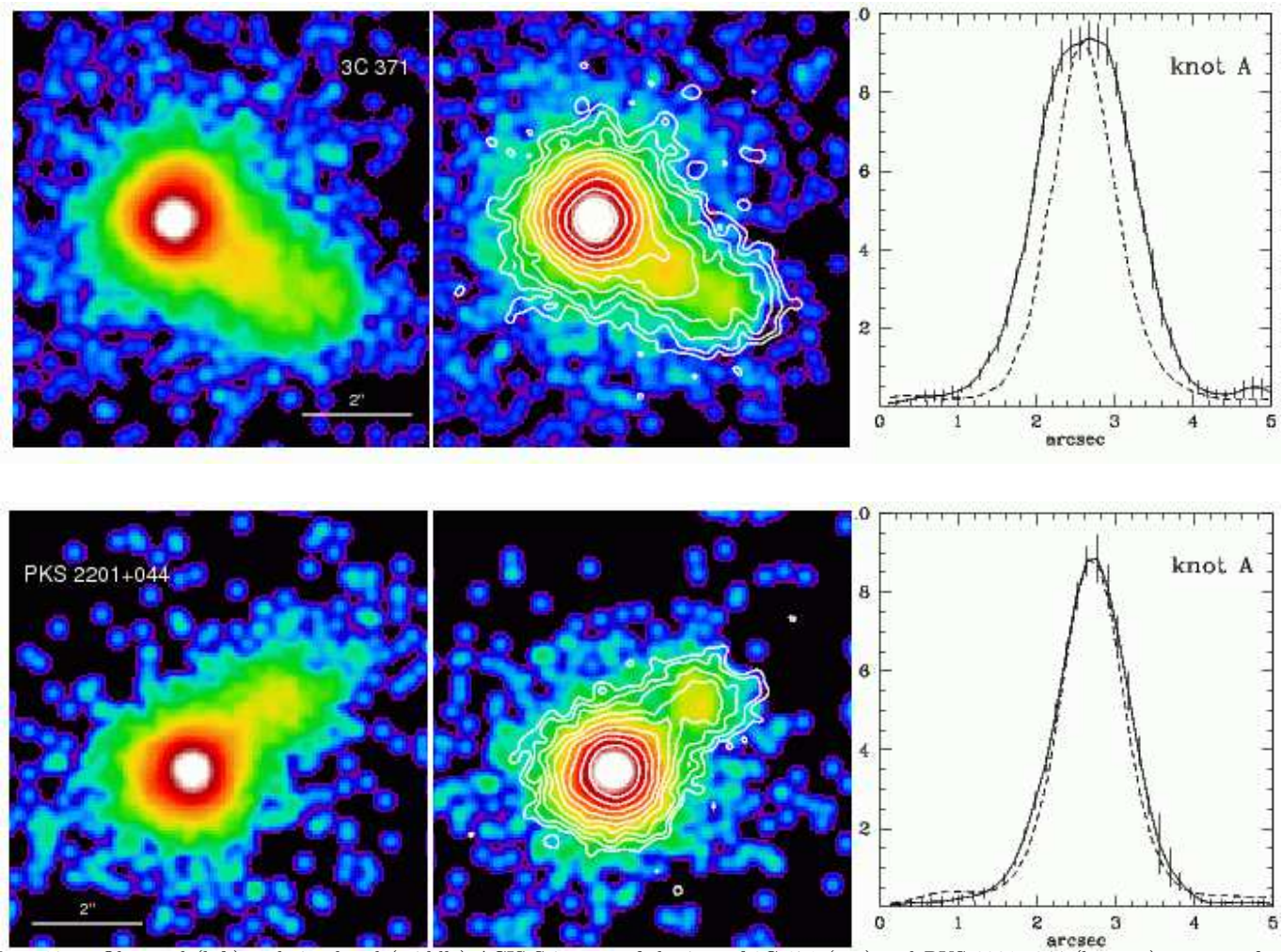

FIG. 12.— Observed (left) and simulated (middle) ACIS-S images of the jets of 3C 371 (top) and PKS 2201+044 (bottom); see text for more details. The contours of the observed images are overlaid on top the simulated ones to show the presence of non-zero X-ray emission from the "edges" of the jets (see text). All images have been rebinned by a factor of 10 (final image pixel of 0.05″) and then smoothed with the *csmooth* in *CIAO* with a circular Gaussian of 0.1″. The right panels show the radial profiles of knots A from the observed (continuous curve with errors) and simulated (dashed) images.

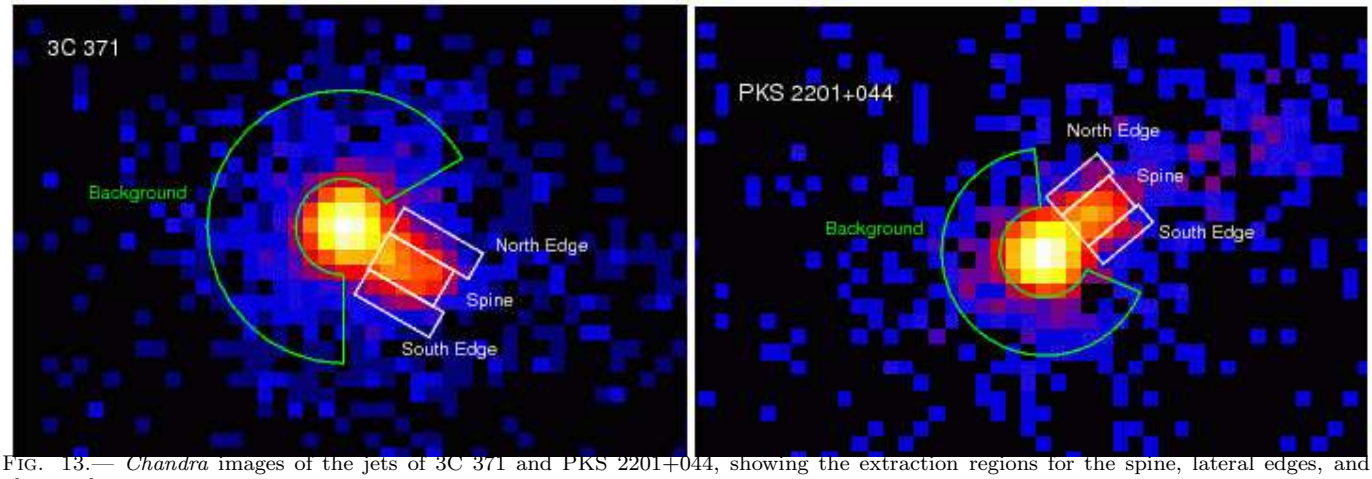

FIG. 13.— *Chandra* images of the jets of 3C 371 and PKS 2201+044, showing the extraction regions for the spine, lateral edges, and background.

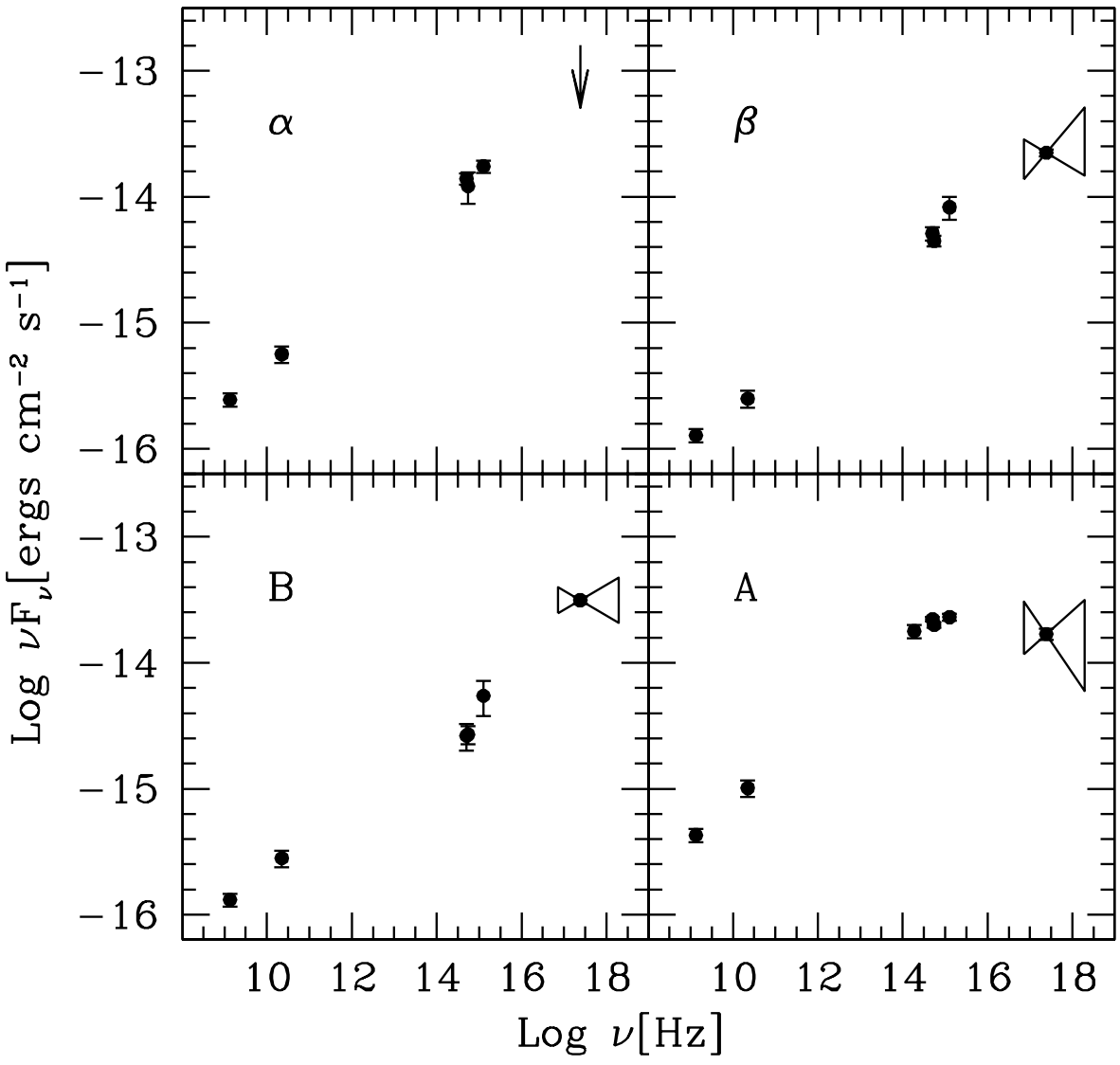

FIG. 14.— Spectral Energy Distributions of the jet knots for 3C 371.

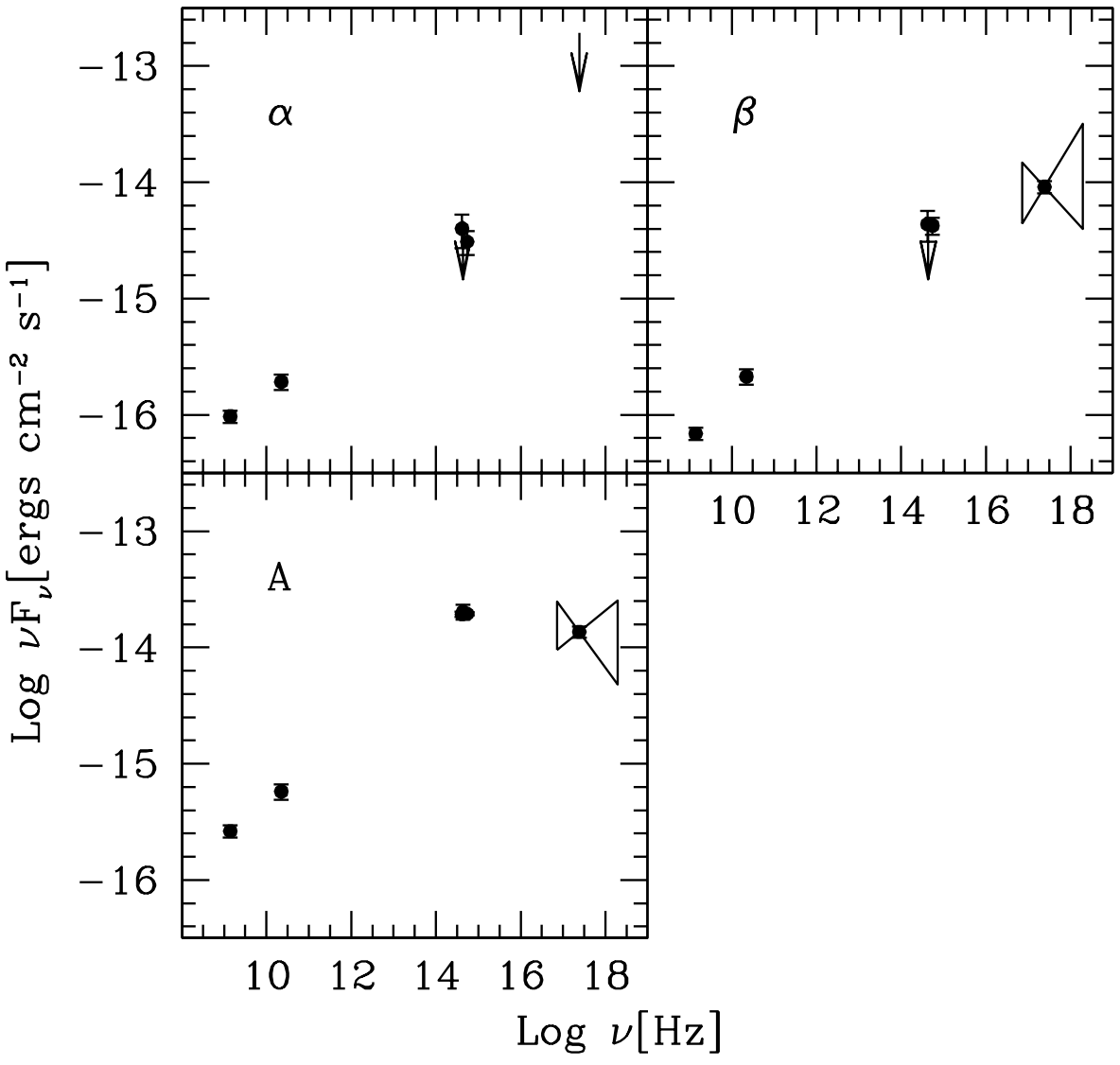

FIG. 15.— Spectral Energy Distributions of the jet knots for PKS 2201+044.

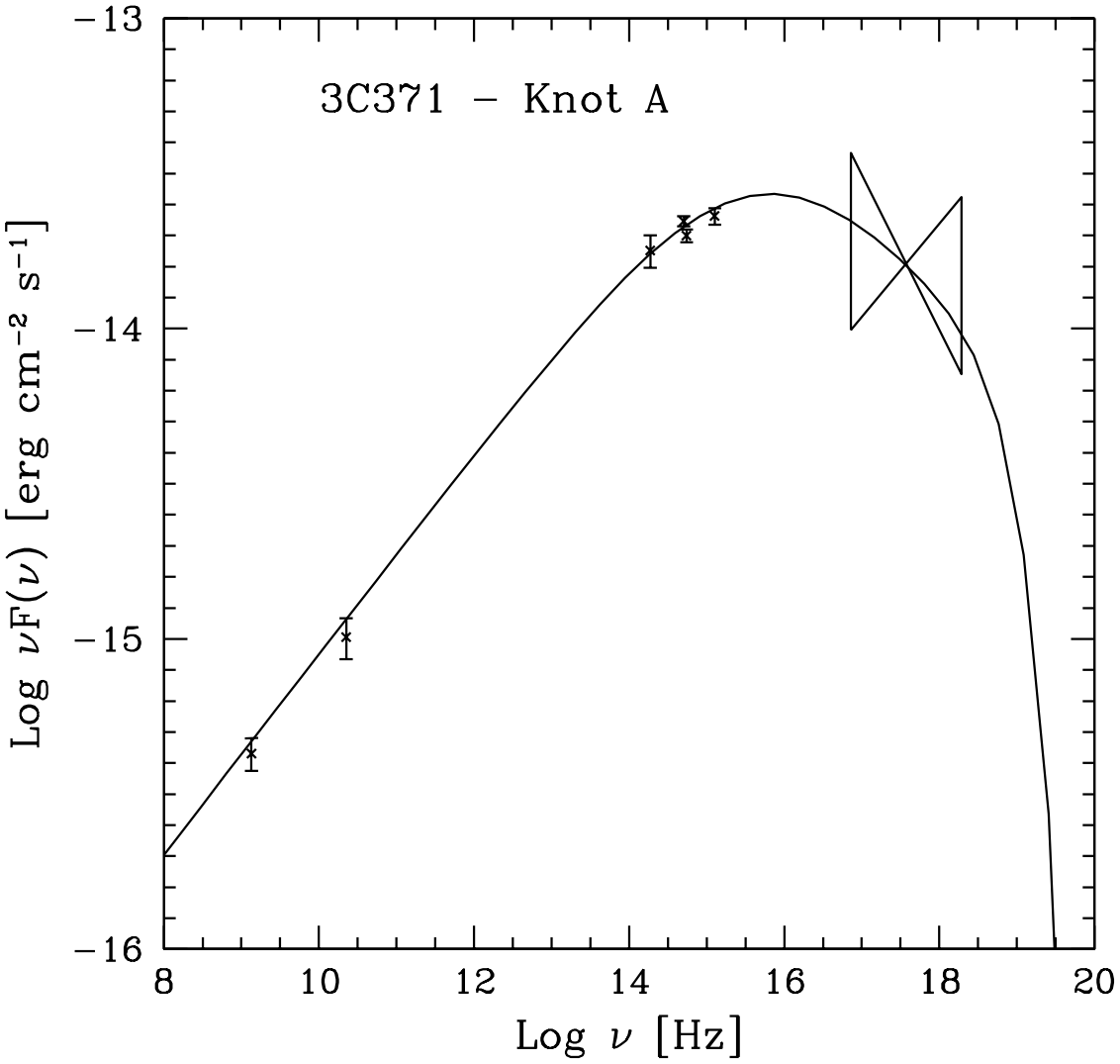

FIG. 16.— Spectral Energy Distributions of the knot A of the 3C 371 jet. The lines are fits to the data with a model assuming synchrotron emission from a broken power law (solid line) distribution of electrons.

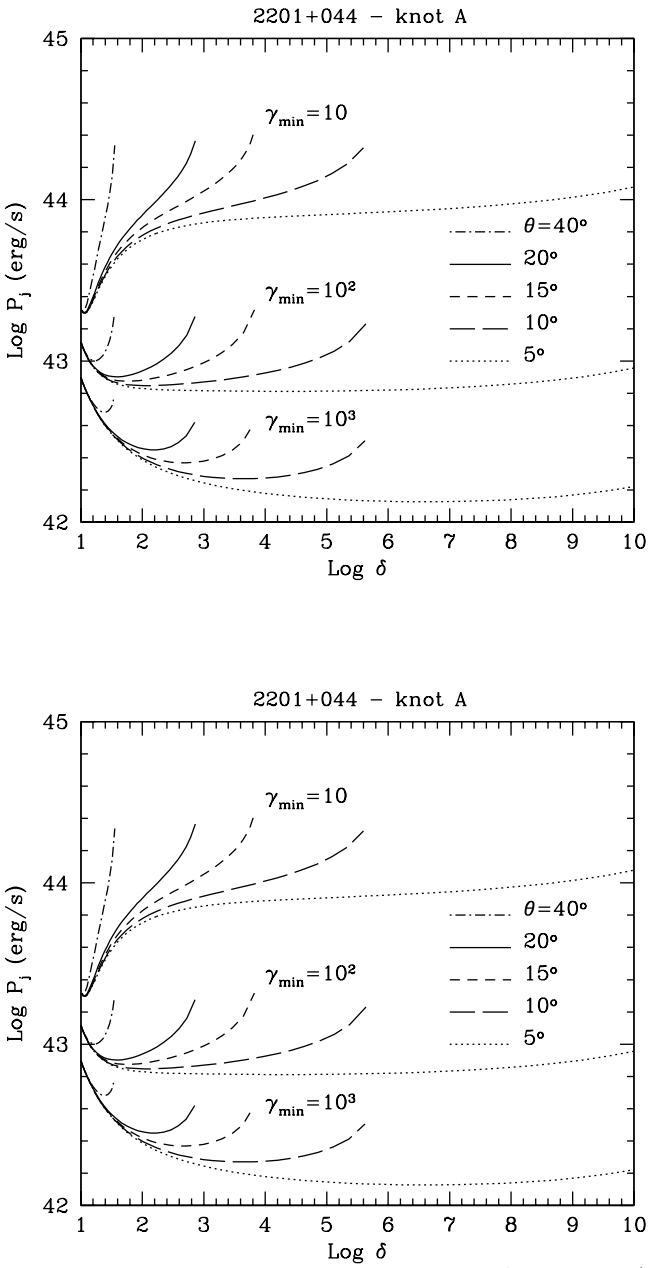

FIG. 17.— Jet kinetic power as a function of the Doppler factor calculated at knots A of 3C 371 (top) and PKS 2201+044 (bottom). The different curves show the power for different values of the minimum Lorentz factor of the relativistic electron, $\gamma_{\rm min}$ and for different jet inclinations (see the text for more details).